instruments

CITESCORE
2.6

Article

Performance of a Modular Ton-Scale Pixel-Readout Liquid Argon Time Projection Chamber

A. Abed Abud, B. Abi, R. Acciarri, M. A. Acero, M. R. Adames, G. Adamov, M. Adamowski, D. Adams, M. Adinolfi, C. Adriano et al.

MDPI

https://doi.org/10.3390/instruments8030041

instruments

MDPI

Article

Performance of a Modular Ton-Scale Pixel-Readout Liquid Argon Time Projection Chamber

A. Abed Abud [1], B. Abi [2], R. Acciarri [3], M. A. Acero [4], M. R. Adames [5], G. Adamov [6], M. Adamowski [3], D. Adams [7], M. Adinolfi [8], C. Adriano [9], A. Aduszkiewicz [10], J. Aguilar [11], B. Aimard [12], F. Akbar [13], K. Allison [14], S. Alonso Monsalve [1], M. Alrashed [15], A. Alton [16], R. Alvarez [17], T. Alves [18], H. Amar [19], P. Amedo [19,20], J. Anderson [21], D. A. Andrade [22], C. Andreopoulos [23], M. Andreotti [24,25], M. P. Andrews [3], F. Andrianala [26], S. Andringa [27], N. Anfimov [28], A. Ankowski [29], M. Antoniassi [5], M. Antonova [19], A. Antoshkin [28], A. Aranda-Fernandez [30], L. Arellano [31], E. Arrieta Diaz [32], M. A. Arroyave [3], J. Asaadi [33], A. Ashkenazi [34], D. Asner [7], L. Asquith [35], E. Atkin [18], D. Auguste [36], A. Aurisano [37], V. Aushev [38], D. Autiero [39], F. Azfar [2], A. Back [40], H. Back [41], J. J. Back [42], I. Bagaturia [6], L. Bagby [3], N. Balashov [28], S. Balasubramanian [3], P. Baldi [43], W. Baldini [24], J. Baldonedo [44], B. Baller [3], B. Bambah [45], R. Banerjee [46], F. Barao [27,47], G. Barenboim [19], P. Ñarham Alzás [1], G. J. Barker [42], W. Barkhouse [48], G. Barr [2], J. Barranco Monarca [49], A. Barros [5], N. Barros [27,50], D. Barrow [2], J. L. Barrow [51], A. Basharina-Freshville [52], A. Bashyal [21], V. Basque [3], C. Batchelor [53], L. Bathe-Peters [2], J. B. R. Battat [54], F. Battisti [2], F. Bay [55], M. C. Q. Bazetto [9], J. L. L. Bazo Alba [56], J. F. Beacom [57], E. Bechetoille [39], B. Behera [58], E. Belchior [59], G. Bell [60], L. Bellantoni [3], G. Bellettini [61,62], V. Bellini [63,64], O. Beltramello [1], N. Benekos [1], C. Benitez Montiel [19,65], D. Benjamin [7], F. Bento Neves [27], J. Berger [66], S. Berkman [67], J. Bernal [65], P. Bernardini [68,69], A. Bersani [70], S. Bertolucci [71,72], M. Betancourt [3], A. Betancur Rodríguez [73], A. Bevan [74], Y. Bezawada [75], A. T. Bezerra [76], T. J. Bezerra [35], A. Bhat [77], V. Bhatnagar [78], J. Bhatt [52], M. Bhattacharjee [79], M. Bhattacharya [3], S. Bhuller [8], B. Bhuyan [79], S. Biagi [80], J. Bian [43], K. Biery [3], B. Bilki [81,82], M. Bishai [7], A. Bitadze [31], A. Blake [83], F. D. Blaszczyk [3], G. C. Blazey [84], E. Blucher [77], J. Bogenschuetz [33], J. Boissevain [85], S. Bolognesi [86], T. Bolton [15], L. Bomben [87,88], M. Bonesini [87,89], C. Bonilla-Diaz [90], F. Bonini [7], A. Booth [74], F. Boran [40], S. Bordoni [1], R. Borges Merlo [9], A. Borkum [35], N. Bostan [82], J. Bracinik [91], D. Braga [3], B. Brahma [92], D. Brailsford [83], F. Bramati [87], A. Branca [87], A. Brandt [33], J. Bremer [1], C. Brew [93], S. J. Brice [3], V. Brio [63], C. Brizzolari [87,89], C. Bromberg [67], J. Brooke [8], A. Bross [3], G. Brunetti [87,89], M. Brunetti [42], N. Buchanan [66], H. Budd [13], J. Buergi [94], D. Burgardt [95], S. Butchart [35], G. Caceres V. [75], I. Cagnoli [71,72], T. Cai [46], R. Calabrese [24,25], J. Calcutt [96], M. Calin [97], L. Calivers [94], E. Calvo [17], A. Caminata [70], A. F. Camino [98], W. Campanelli [27], A. Campani [70,99], A. Campos Benitez [100], N. Canci [101], J. Capó [19], I. Caracas [102], D. Caratelli [103], D. Carber [66], J. M. Carceller [1], G. Carini [7], B. Carlus [39], M. F. Carneiro [7], P. Carniti [87], I. Caro Terrazas [66], H. Carranza [33], N. Carrara [75], L. Carroll [15], T. Carroll [104], A. Carter [105], E. Casarejos [44], D. Casazza [24], J. F. Castaño Forero [106], F. A. Castaño [107], A. Castillo [108], C. Castromonte [109], E. Catano-Mur [110], C. Cattadori [87], F. Cavalier [36], F. Cavanna [3], S. Centro [111], G. Cerati [3], C. Cerna [112], A. Cervelli [71], A. Cervera Villanueva [19], K. Chakraborty [113], S. Chakraborty [114], M. Chalifour [1], A. Chappell [42], N. Charitonidis [1], A. Chatterjee [113], H. Chen [7], M. Chen [43], W. C. Chen [115], Y. Chen [29], Z. Chen-Wishart [105], D. Cherdack [10], C. Chi [116], R. Chirco [22], N. Chitirasreemadam [61,62], K. Cho [117], S. Choate [84], D. Chokheli [6], P. S. Chong [118], B. Chowdhury [21], D. Christian [3], A. Chukanov [28], M. Chung [119], E. Church [41], M. F. Cicala [52], M. Cicerchia [111], V. Cicero [71,72], R. Ciolini [61], P. Clarke [53], G. Cline [11], T. E. Coan [120], A. G. Cocco [101], J. A. B. Coelho [121], A. Cohen [121], J. Collazo [44], J. Collot [122], E. Conley [123], J. M. Conrad [51], M. Convery [29], S. Copello [70], P. Cova [124,125], C. Cox [105], L. Cremaldi [126], L. Cremonesi [74], J. I. Crespo-Anadón [17], M. Crisler [3], E. Cristaldo [65,87], J. Crnkovic [3], G. Crone [52], R. Cross [42], A. Cudd [14], C. Cuesta [17], Y. Cui [127], F. Curciarello [128], D. Cussans [8], J. Dai [122], O. Dalager [43], R. Dallavalle [121], W. Dallaway [115], H. da Motta [129], Z. A. Dar [110], R. Darby [35], L. Da Silva Peres [130], Q. David [39], G. S. Davies [126], S. Davini [70],

check for updates

Citation: Abed Abud, A.; Abi, B.; Acciarri, R.; Acero, M.A.; Adames, M.R.; Adamov, G.; Adamowski, M.; Adams, D.; Adinolfi, M.; Adriano, C.; et al. Performance of a Modular Ton-Scale Pixel-Readout Liquid Argon Time Projection Chamber. *Instruments* **2024**, *8*, 41. https://doi.org/10.3390/instruments8030041

Academic Editor: Pasquale Arpaia

Received: 8 March 2024
Revised: 6 June 2024
Accepted: 26 August 2024
Published: 11 September 2024

J. Dawson [121], R. De Aguiar [9], P. De Almeida [9], P. Debbins [82], I. De Bonis [12], M. P. Decowski [131,132], A. de Gouvêa [133], P. C. De Holanda [9], I. L. De Icaza Astiz [35], P. De Jong [131,132], P. Del Amo Sanchez [12], A. De la Torre [17], G. De Lauretis [39], A. Delbart [86], D. Delepine [49], M. Delgado [87,89], A. Dell'Acqua [1], G. Delle Monache [128], N. Delmonte [124,125], P. De Lurgio [21], R. Demario [67], G. De Matteis [68], J. R. T. de Mello Neto [130], D. M. DeMuth [134], S. Dennis [135], C. Densham [93], P. Denton [7], G. W. Deptuch [7], A. De Roeck [1], V. De Romeri [19], J. P. Detje [135], J. Devine [1], R. Dharmapalan [136], M. Dias [137], A. Diaz [138], J. S. Díaz [40], F. Díaz [56], F. Di Capua [101,139], A. Di Domenico [140,141], S. Di Domizio [70,99], S. Di Falco [61], L. Di Giulio [1], P. Ding [3], L. Di Noto [70,99], E. Diociaiuti [128], C. Distefano [80], R. Diurba [94], M. Diwan [7], Z. Djurcic [21], D. Doering [29], S. Dolan [1], F. Dolek [100], M. J. Dolinski [142], D. Domenici [128], L. Domine [29], S. Donati [61,62], Y. Donon [1], S. Doran [143], D. Douglas [29], T. A. Doyle [144], A. Dragone [29], F. Drielsma [29], L. Duarte [137], D. Duchesneau [12], K. Duffy [2,3], K. Dugas [43], P. Dunne [18], B. Dutta [145], H. Duyang [146], D. A. Dwyer [11], A. S. Dyshkant [84], S. Dytman [98], M. Eads [84], A. Earle [35], S. Edayath [143], D. Edmunds [67], J. Eisch [3], P. Englezos [147], A. Ereditato [77], T. Erjavec [75], C. O. Escobar [3], J. J. Evans [31], E. Ewart [40], A. C. Ezeribe [148], K. Fahey [3], L. Fajt [1], A. Falcone [87,89], M. Fani' [85], C. Farnese [149], S. Farrell [150], Y. Farzan [151], D. Fedoseev [28], J. Felix [49], Y. Feng [143], E. Fernandez-Martinez [152], G. Ferry [36], L. Fields [153], P. Filip [154], A. Filkins [155], F. Filthaut [131,156], R. Fine [85], G. Fiorillo [101,139], M. Fiorini [24,25], S. Fogarty [66], W. Foreman [22], J. Fowler [123], J. Franc [157], K. Francis [84], D. Franco [77], J. Franklin [158], J. Freeman [3], J. Fried [7], A. Friedland [29], S. Fuess [3], I. K. Furic [58], K. Furman [74], A. P. Furmanski [159], R. Gaba [78], A. Gabrielli [71,72], A. M. Gago [56], F. Galizzi [87], H. Gallagher [160], A. Gallas [36], N. Gallice [7], V. Galymov [39], E. Gamberini [1], T. Gamble [148], F. Ganacim [5], R. Gandhi [161], S. Ganguly [3], F. Gao [103], S. Gao [7], D. Garcia-Gamez [162], M. Á. García-Peris [19], F. Gardim [76], S. Gardiner [3], D. Gastler [163], A. Gauch [94], J. Gauvreau [164], P. Gauzzi [140,141], S. Gazzana [128], G. Ge [116], N. Geffroy [12], B. Gelli [9], S. Gent [165], L. Gerlach [7], Z. Ghorbani-Moghaddam [70], T. Giammaria [24,25], D. Gibin [111,149], I. Gil-Botella [17], S. Gilligan [96], A. Gioiosa [61], S. Giovannella [128], C. Girerd [39], A. K. Giri [92], C. Giugliano [24], V. Giusti [61], D. Gnani [11], O. Gogota [38], S. Gollapinni [85], K. Gollwitzer [3], R. A. Gomes [166], L. V. Gomez Bermeo [108], L. S. Gomez Fajardo [108], F. Gonnella [91], D. Gonzalez-Diaz [20], M. Gonzalez-Lopez [152], M. C. Goodman [21], S. Goswami [113], C. Gotti [87], J. Goudeau [59], E. Goudzovski [91], C. Grace [11], E. Gramellini [31], R. Gran [167], E. Granados [49], P. Granger [121], C. Grant [163], D. R. Gratieri [9,168], G. Grauso [101], P. Green [2], S. Greenberg [11,169], J. Greer [8], W. C. Griffith [35], F. T. Groetschla [1], K. Grzelak [170], L. Gu [83], W. Gu [7], V. Guarino [21], M. Guarise [24,25], R. Guenette [31], E. Guerard [36], M. Guerzoni [71], D. Guffanti [87,89], A. Guglielmi [149], B. Guo [146], Y. Guo [144], A. Gupta [29], V. Gupta [131,132], G. Gurung [33], D. Gutierrez [171], P. Guzowski [31], M. M. Guzzo [9], S. Gwon [172], A. Habig [167], H. Hadavand [33], L. Haegel [39], R. Haenni [94], L. Hagaman [173], A. Hahn [3], J. Haiston [174], J. Hakenmueller [123], T. Hamernik [3], P. Hamilton [18], J. Hancock [91], F. Happacher [128], D. A. Harris [3,46], J. Hartnell [35], T. Hartnett [93], J. Harton [66], T. Hasegawa [175], C. Hasnip [2], R. Hatcher [3], K. Hayrapetyan [74], J. Hays [74], E. Hazen [163], M. He [10], A. Heavey [3], K. M. Heeger [173], J. Heise [176], S. Henry [13], M. A. Hernandez Morquecho [22], K. Herner [3], V. Hewes [37], A. Higuera [150], C. Hilgenberg [159], S. J. Hillier [91], A. Himmel [3], E. Hinkle [77], L. R. Hirsch [5], J. Ho [177], J. Hoff [3], A. Holin [93], T. Holvey [2], E. Hoppe [41], S. Horiuchi [100], G. A. Horton-Smith [15], M. Hostert [159], T. Houdy [36], B. Howard [3], R. Howell [13], I. Hristova [93], M. S. Hronek [3], J. Huang [75], R. G. Huang [11], Z. Hulcher [29], M. Ibrahim [178], G. Iles [18], N. Ilic [115], A. M. Iliescu [128], R. Illingworth [3], G. Ingratta [71,72], A. Ioannisian [179], B. Irwin [159], L. Isenhower [180], M. Ismerio Oliveira [130], R. Itay [29], C. M. Jackson [41], V. Jain [181], E. James [3], W. Jang [33], B. Jargowsky [43], D. Jena [3], I. Jentz [104], X. Ji [7], C. Jiang [182], J. Jiang [144], L. Jiang [100], A. Jipa [97], F. R. Joaquim [27,47], W. Johnson [174], C. Jollet [112], B. Jones [33], R. Jones [148], D. José Fernández [20], N. Jovancevic [183], M. Judah [98], C. K. Jung [144], T. Junk [3], Y. Jwa [29,116], M. Kabirnezhad [18], A. C. Kaboth [93,105], I. Kadenko [38], I. Kakorin [28], A. Kalitkina [28], D. Kalra [116], M. Kandemir [184], D. M. Kaplan [22], G. Karagiorgi [116], G. Karaman [82], A. Karcher [11], Y. Karyotakis [12], S. Kasai [185], S. P. Kasetti [59], L. Kashur [66], I. Katsioulas [91], A. Kauther [84], N. Kazaryan [179],

L. Ke [7], E. Kearns [163], P. T. Keener [118], K. J. Kelly [1], E. Kemp [9], O. Kemularia [6], Y. Kermaidic [36], W. Ketchum [3], S. H. Kettell [7], M. Khabibullin [28], N. Khan [18], A. Khvedelidze [6], D. Kim [145], J. Kim [13], M. Kim [3], B. King [3], B. Kirby [116], M. Kirby [7], A. Kish [3], J. Klein [118], J. Kleykamp [126], A. Klustova [18], T. Kobilarcik [3], L. Koch [102], K. Koehler [104], L. W. Koerner [10], D. H. Koh [29], L. Kolupaeva [28], D. Korablev [28], M. Kordosky [110], T. Kosc [122], U. Kose [1], V. A. Kostelecký [40], K. Kothekar [8], I. Kotler [142], M. Kovalcuk [154], V. Kozhukalov [28], W. Krah [131], R. Kralik [35], M. Kramer [11], L. Kreczko [8], F. Krennrich [143], I. Kreslo [94], T. Kroupova [118], S. Kubota [31], M. Kubu [1], Y. Kudenko [28], V. A. Kudryavtsev [148], G. Kufatty [186], S. Kuhlmann [21], J. Kumar [136], P. Kumar [148], S. Kumaran [43], P. Kunze [12], J. Kunzmann [94], R. Kuravi [11], N. Kurita [29], C. Kuruppu [146], V. Kus [157], T. Kutter [59], J. Kvasnicka [154], T. Labree [84], T. Lackey [3], A. Lambert [11], B. J. Land [118], C. E. Lane [142], N. Lane [31], K. Lang [187], T. Langford [173], M. Langstaff [31], F. Lanni [1], O. Lantwin [12], J. Larkin [7], P. Lasorak [18], D. Last [118], A. Laudrain [102], A. Laundrie [104], G. Laurenti [71], E. Lavaut [36], A. Lawrence [11], P. Laycock [7], I. Lazanu [97], M. Lazzaroni [124,188], T. Le [160], S. Leardini [20], J. Learned [136], T. LeCompte [29], C. Lee [3], V. Legin [38], G. Lehmann Miotto [1], R. Lehnert [40], M. A. Leigui de Oliveira [189], M. Leitner [11], D. Leon Silverio [174], L. M. Lepin [31,186], J.-Y. Li [53], S. W. Li [75], Y. Li [7], H. Liao [15], C. S. Lin [11], D. Lindebaum [8], S. Linden [7], R. A. Lineros [90], J. Ling [190], A. Lister [104], B. R. Littlejohn [22], H. Liu [7], J. Liu [43], Y. Liu [77], S. Lockwitz [3], M. Lokajicek [154], I. Lomidze [6], K. Long [18], T. V. Lopes [76], J. Lopez [107], I. López de Rego [17], N. López-March [19], T. Lord [42], J. M. LoSecco [153], W. C. Louis [85], A. Lozano Sanchez [142], X.-G. Lu [42], K. B. Luk [169,191], B. Lunday [118], X. Luo [103], E. Luppi [24,25], J. Maalmi [36], D. MacFarlane [29], A. A. Machado [9], P. Machado [3], C. T. Macias [40], J. R. Macier [3], M. MacMahon [52], A. Maddalena [192], A. Madera [1], P. Madigan [11,169], S. Magill [21], C. Magueur [36], K. Mahn [67], A. Maio [27,50], A. Major [123], K. Majumdar [23], M. Man [115], R. C. Mandujano [43], J. Maneira [27,50], S. Manly [13], A. Mann [160], K. Manolopoulos [93], M. Manrique Plata [40], S. Manthey Corchado [17], V. N. Manyam [7], M. Marchan [3], A. Marchionni [3], W. Marciano [7], D. Marfatia [136], C. Mariani [100], J. Maricic [136], F. Marinho [193], A. D. Marino [14], T. Markiewicz [29], F. Das Chagas Marques [9], C. Marquet [112], D. Marsden [31], M. Marshak [159], C. M. Marshall [13], J. Marshall [42], L. Martina [68], J. Martín-Albo [19], N. Martinez [15], D. A. Martinez Caicedo [174], F. Martínez López [74], P. Martínez Miravé [19], S. Martynenko [7], V. Mascagna [87], C. Massari [87], A. Mastbaum [147], F. Matichard [11], S. Matsuno [136], G. Matteucci [101,139], J. Matthews [59], C. Mauger [118], N. Mauri [71,72], K. Mavrokoridis [23], I. Mawby [83], R. Mazza [87], A. Mazzacane [3], T. McAskill [54], N. McConkey [52], K. S. McFarland [13], C. McGrew [144], A. McNab [31], L. Meazza [87], V. C. N. Meddage [58], B. Mehta [78], P. Mehta [194], P. Melas [195], O. Mena [19], H. Mendez [171], P. Mendez [1], D. P. Méndez [7], A. Menegolli [196,197], G. Meng [149], A. C. E. A. Mercuri [5], A. Meregaglia [112], M. D. Messier [40], S. Metallo [159], J. Metcalf [51,160], W. Metcalf [59], M. Mewes [40], H. Meyer [95], T. Miao [3], A. Miccoli [68], G. Michna [165], V. Mikola [52], R. Milincic [136], F. Miller [104], G. Miller [31], W. Miller [159], O. Mineev [28], A. Minotti [87,89], L. Miralles [1], O. G. Miranda [198], C. Mironov [121], S. Miryala [7], S. Miscetti [128], C. S. Mishra [3], S. R. Mishra [146], A. Mislivec [159], M. Mitchell [59], D. Mladenov [1], I. Mocioiu [199], A. Mogan [3], N. Moggi [71,72], R. Mohanta [45], T. A. Mohayai [40], N. Mokhov [3], J. Molina [65], L. Molina Bueno [19], E. Montagna [71,72], A. Montanari [71], C. Montanari [3,196,197], D. Montanari [3], D. Montanino [68,69], L. M. Montaño Zetina [198], M. Mooney [66], A. F. Moor [148], Z. Moore [155], D. Moreno [106], O. Moreno-Palacios [110], L. Morescalchi [61], D. Moretti [87], R. Moretti [87], C. Morris [10], C. Mossey [3], M. Mote [59], C. A. Moura [189], G. Mouster [83], W. Mu [3], L. Mualem [138], J. Mueller [66], M. Muether [95], F. Muheim [53], A. Muir [60], M. Mulhearn [75], D. Munford [10], L. J. Munteanu [1], H. Muramatsu [159], J. Muraz [122], M. Murphy [100], T. Murphy [155], J. Muse [159], A. Mytilinaki [93], J. Nachtman [82], Y. Nagai [178], S. Nagu [200], R. Nandakumar [93], D. Naples [98], S. Narita [201], A. Nath [79], A. Navrer-Agasson [31], N. Nayak [7], M. Nebot-Guinot [53], A. Nehm [102], J. K. Nelson [110], O. Neogi [82], J. Nesbit [104], M. Nessi [1,3], D. Newbold [93], M. Newcomer [118], R. Nichol [52], F. Nicolas-Arnaldos [162], A. Nikolica [118], J. Nikolov [183], E. Niner [3], K. Nishimura [136], A. Norman [3], A. Norrick [3], P. Novella [19], J. A. Nowak [83], M. Oberling [21], J. P. Ochoa-Ricoux [43], S. Oh [123], S. B. Oh [3], A. Olivier [153], A. Olshevskiy [28], T. Olson [10], Y. Onel [82], Y. Onishchuk [38], A. Oranday [40],

M. Osbiston [42], J. A. Osorio Vélez [107], L. Otiniano Ormachea [109,202], J. Ott [43], L. Pagani [75], G. Palacio [73], O. Palamara [3], S. Palestini [1], J. M. Paley [3], M. Pallavicini [70,99], C. Palomares [17], S. Pan [113], P. Panda [45], W. Panduro Vazquez [105], E. Pantic [75], V. Paolone [98], V. Papadimitriou [3], R. Papaleo [80], A. Papanestis [93], D. Papoulias [195], S. Paramesvaran [8], A. Paris [171], S. Parke [3], E. Parozzi [87,89], S. Parsa [94], Z. Parsa [7], S. Parveen [194], M. Parvu [97], D. Pasciuto [61], S. Pascoli [71,72], L. Pasqualini [71,72], J. Pasternak [18], C. Patrick [52,53], L. Patrizii [71], R. B. Patterson [138], T. Patzak [121], A. Paudel [3], L. Paulucci [189], Z. Pavlovic [3], G. Pawloski [159], D. Payne [23], V. Pec [154], E. Pedreschi [61], S. J. M. Peeters [35], W. Pellico [3], A. Pena Perez [29], E. Pennacchio [39], A. Penzo [82], O. L. G. Peres [9], Y. F. Perez Gonzalez [158], L. Pérez-Molina [17], C. Pernas [110], J. Perry [53], D. Pershey [186], G. Pessina [87], G. Petrillo [29], C. Petta [63,64], R. Petti [146], M. Pfaff [18], V. Pia [71,72], L. Pickering [93,105], F. Pietropaolo [1,149], V. L. Pimentel [9,203], G. Pinaroli [7], J. Pinchault [12], K. Pitts [100], K. Plows [2], R. Plunkett [3], C. Pollack [171], T. Pollman [131,132], D. Polo-Toledo [4], F. Pompa [19], X. Pons [1], N. Poonthottathil [114,143], V. Popov [34], F. Poppi [71,72], J. Porter [35], M. Potekhin [7], R. Potenza [63,64], J. Pozimski [18], M. Pozzato [71,72], T. Prakash [11], C. Pratt [75], M. Prest [87], F. Psihas [3], D. Pugnere [39], X. Qian [7], J. L. Raaf [3], V. Radeka [7], J. Rademacker [8], B. Radics [46], A. Rafique [21], E. Raguzin [7], M. Rai [42], S. Rajagopalan [7], M. Rajaoalisoa [37], I. Rakhno [3], L. Rakotondravohitra [26], L. Ralte [92], M. A. Ramirez Delgado [118], B. Ramson [3], A. Rappoldi [196,197], G. Raselli [196,197], P. Ratoff [83], R. Ray [3], H. Razafinime [37], E. M. Rea [159], J. S. Real [122], B. Rebel [3,104], R. Rechenmacher [3], M. Reggiani-Guzzo [31], J. Reichenbacher [174], S. D. Reitzner [3], H. Rejeb Sfar [1], E. Renner [85], A. Renshaw [10], S. Rescia [7], F. Resnati [1], D. Restrepo [107], C. Reynolds [74], M. Ribas [5], S. Riboldi [124], C. Riccio [144], G. Riccobene [80], J. S. Ricol [122], M. Rigan [35], E. V. Rincón [73], A. Ritchie-Yates [105], S. Ritter [102], D. Rivera [85], R. Rivera [3], A. Robert [122], J. L. Rocabado Rocha [19], L. Rochester [29], M. Roda [23], P. Rodrigues [2], M. J. Rodriguez Alonso [1], J. Rodriguez Rondon [174], S. Rosauro-Alcaraz [36], P. Rosier [36], D. Ross [67], M. Rossella [196,197], M. Rossi [1], M. Ross-Lonergan [85], N. Roy [46], P. Roy [95], C. Rubbia [204], A. Ruggeri [71], G. Ruiz Ferreira [31], B. Russell [51], D. Ruterbories [13], A. Rybnikov [28], A. Saa-Hernandez [20], R. Saakyan [52], S. Sacerdoti [121], S. K. Sahoo [92], N. Sahu [92], P. Sala [1,124], N. Samios [7], O. Samoylov [28], M. C. Sanchez [186], A. Sánchez Bravo [19], P. Sanchez-Lucas [162], V. Sandberg [85], D. A. Sanders [126], S. Sanfilippo [80], D. Sankey [93], D. Santoro [124], N. Saoulidou [195], P. Sapienza [80], C. Sarasty [37], I. Sarcevic [205], I. Sarra [128], G. Savage [3], V. Savinov [98], G. Scanavini [173], A. Scaramelli [196], A. Scarff [148], T. Schefke [59], H. Schellman [3,96], S. Schifano [24,25], P. Schlabach [3], D. Schmitz [77], A. W. Schneider [51], K. Scholberg [123], A. Schukraft [3], B. Schuld [14], A. Segade [44], E. Segreto [9], A. Selyunin [28], C. R. Senise [137], J. Sensenig [118], M. H. Shaevitz [116], P. Shanahan [3], P. Sharma [78], R. Kumar [206], K. Shaw [35], T. Shaw [3], K. Shchablo [39], J. Shen [118], C. Shepherd-Themistocleous [93], A. Sheshukov [28], W. Shi [144], S. Shin [207], S. Shivakoti [95], I. Shoemaker [100], D. Shooltz [67], R. Shrock [144], B. Siddi [24], M. Siden [66], J. Silber [11], L. Simard [36], J. Sinclair [29], G. Sinev [174], Jaydip Singh [200], J. Singh [200], L. Singh [208], P. Singh [74], V. Singh [208], S. Singh Chauhan [78], R. Sipos [1], C. Sironneau [121], G. Sirri [71], K. Siyeon [172], K. Skarpaas [29], J. Smedley [13], E. Smith [40], J. Smith [144], P. Smith [40], J. Smolik [154,157], M. Smy [43], M. Snape [42], E. L. Snider [3], P. Snopok [22], D. Snowden-Ifft [164], M. Soares Nunes [3], H. Sobel [43], M. Soderberg [155], S. Sokolov [28], C. J. Solano Salinas [109,209], S. Söldner-Rembold [31], S. R. Soleti [11], N. Solomey [95], V. Solovov [27], W. E. Sondheim [85], M. Sorel [19], A. Sotnikov [28], J. Soto-Oton [19], A. Sousa [37], K. Soustruznik [210], F. Spinella [61], J. Spitz [211], N. J. C. Spooner [148], K. Spurgeon [155], D. Stalder [65], M. Stancari [3], L. Stanco [111,149], J. Steenis [75], R. Stein [8], H. M. Steiner [11], A. F. Steklain Lisbôa [5], A. Stepanova [28], J. Stewart [7], B. Stillwell [77], J. Stock [174], F. Stocker [1], T. Stokes [59], M. Strait [159], T. Strauss [3], L. Strigari [145], A. Stuart [30], J. G. Suarez [73], J. Subash [91], A. Surdo [68], L. Suter [3], C. M. Sutera [63,64], K. Sutton [138], Y. Suvorov [101,139], R. Svoboda [75], S. K. Swain [212], B. Szczerbinska [213], A. M. Szelc [53], A. Sztuc [52], A. Taffara [61], N. Talukdar [146], J. Tamara [106], H. A. Tanaka [29], S. Tang [7], N. Taniuchi [135], A. M. Tapia Casanova [214], B. Tapia Oregui [187], A. Tapper [18], S. Tariq [3], E. Tarpara [7], E. Tatar [215], R. Tayloe [40], D. Tedeschi [146], A. M. Teklu [144], J. Tena Vidal [34],

P. Tennessen [11,55], M. Tenti [71], K. Terao [29], F. Terranova [87,89], G. Testera [70], T. Thakore [37], A. Thea [93], A. Thiebault [36], S. Thomas [155], A. Thompson [145], C. Thorn [7], S. C. Timm [3], E. Tiras [82,184], V. Tishchenko [7], N. Todorović [183], L. Tomassetti [24,25], A. Tonazzo [121], D. Torbunov [7], M. Torti [87], M. Tortola [19], F. Tortorici [63,64], N. Tosi [71], D. Totani [103], M. Toups [3], C. Touramanis [23], D. Tran [10], R. Travaglini [71], J. Trevor [138], E. Triller [67], S. Trilov [8], J. Truchon [104], D. Truncali [140,141], W. H. Trzaska [216], Y. Tsai [43], Y.-T. Tsai [29], Z. Tsamalaidze [6], K. V. Tsang [29], N. Tsverava [6], S. Z. Tu [182], S. Tufanli [1], C. Tunnell [150], J. Turner [158], M. Tuzi [19], J. Tyler [15], E. Tyley [148], M. Tzanov [59], M. A. Uchida [135], J. Ureña González [19], J. Urheim [40], T. Usher [29], H. Utaegbulam [13], S. Uzunyan [84], M. R. Vagins [43,217], P. Vahle [110], S. Valder [35], G. A. Valdiviesso [76], E. Valencia [49], R. Valentim [137], Z. Vallari [138], E. Vallazza [87], J. W. F. Valle [19], R. Van Berg [118], R. G. Van de Water [85], D. V. Forero [214], A. Vannozzi [128], M. Van Nuland-Troost [131], F. Varanini [149], D. Vargas Oliva [115], S. Vasina [28], N. Vaughan [96], K. Vaziri [3], A. Vázquez-Ramos [162], J. Vega [202], S. Ventura [149], A. Verdugo [17], S. Vergani [52], M. Verzocchi [3], K. Vetter [3], M. Vicenzi [7], H. Vieira de Souza [121], C. Vignoli [192], C. Vilela [27], E. Villa [1], S. Viola [80], B. Viren [7], A. Vizcaya-Hernandez [66], T. Vrba [157], Q. Vuong [13], A. V. Waldron [74], M. Wallbank [37], J. Walsh [67], T. Walton [3], H. Wang [218], J. Wang [174], L. Wang [11], M. H. L. S. Wang [3], X. Wang [3], Y. Wang [218], K. Warburton [143], D. Warner [66], L. Warsame [18], M. O. Wascko [2], D. Waters [52], A. Watson [91], K. Wawrowska [35,93], A. Weber [3,102], C. M. Weber [159], M. Weber [94], H. Wei [59], A. Weinstein [143], H. Wenzel [3], S. Westerdale [127], M. Wetstein [143], K. Whalen [93], J. Whilhelmi [173], A. White [33], A. White [173], L. H. Whitehead [135], D. Whittington [155], M. J. Wilking [159], A. Wilkinson [52], C. Wilkinson [11], F. Wilson [93], R. J. Wilson [66], P. Winter [21], W. Wisniewski [29], J. Wolcott [160], J. Wolfs [13], T. Wongjirad [160], A. Wood [10], K. Wood [11], E. Worcester [7], M. Worcester [7], M. Wospakrik [3], K. Wresilo [135], C. Wret [13], S. Wu [159], W. Wu [3], W. Wu [43], M. Wurm [102], J. Wyenberg [177], Y. Xiao [43], I. Xiotidis [18], B. Yaeggy [37], N. Yahlali [19], E. Yandel [103], K. Yang [2], T. Yang [3], A. Yankelevich [43], N. Yershov [28], K. Yonehara [3], T. Young [48], B. Yu [7], H. Yu [7], J. Yu [33], Y. Yu [22], W. Yuan [53], R. Zaki [46], J. Zalesak [154], L. Zambelli [12], B. Zamorano [162], A. Zani [124], O. Zapata [107], L. Zazueta [155], G. P. Zeller [3], J. Zennamo [3], K. Zeug [104], C. Zhang [7], S. Zhang [40], M. Zhao [7], E. Zhivun [7], E. D. Zimmerman [14], S. Zucchelli [71,72], J. Zuklin [154], V. Zutshi [84], R. Zwaska [3] and on behalf of the DUNE Collaboration [*,†]

1 CERN, The European Organization for Nuclear Research, 1211 Meyrin, Switzerland
2 University of Oxford, Oxford OX1 3RH, UK
3 Fermi National Accelerator Laboratory, Batavia, IL 60510, USA
4 Universidad del Atlántico, Barranquilla, Atlántico, Colombia
5 Universidade Tecnológica Federal do Paraná, Curitiba, Brazil
6 Georgian Technical University, Tbilisi, Georgia
7 Brookhaven National Laboratory, Upton, NY 11973, USA
8 University of Bristol, Bristol BS8 1TL, UK
9 Universidade Estadual de Campinas, Campinas 13083-970, SP, Brazil
10 University of Houston, Houston, TX 77204, USA
11 Lawrence Berkeley National Laboratory, Berkeley, CA 94720, USA
12 Laboratoire d'Annecy de Physique des Particules, Université Savoie Mont Blanc, CNRS, LAPP-IN2P3, 74000 Annecy, France
13 University of Rochester, Rochester, NY 14627, USA
14 University of Colorado Boulder, Boulder, CO 80309, USA
15 Kansas State University, Manhattan, KS 66506, USA
16 Augustana University, Sioux Falls, SD 57197, USA
17 CIEMAT, Centro de Investigaciones Energéticas, Medioambientales y Tecnológicas, E-28040 Madrid, Spain
18 Imperial College of Science Technology and Medicine, London SW7 2BZ, UK
19 Instituto de Física Corpuscular, CSIC and Universitat de València, 46980 Paterna, Valencia, Spain
20 Instituto Galego de Física de Altas Enerxías, University of Santiago de Compostela, 15782 Santiago de Compostela, Spain
21 Argonne National Laboratory, Argonne, IL 60439, USA
22 Illinois Institute of Technology, Chicago, IL 60616, USA
23 University of Liverpool, Liverpool L69 7ZE, UK
24 Istituto Nazionale di Fisica Nucleare Sezione di Ferrara, I-44122 Ferrara, Italy

[25] University of Ferrara, Ferrara, Italy
[26] University of Antananarivo, Antananarivo 101, Madagascar
[27] Laboratório de Instrumentação e Física Experimental de Partículas, 1649-003 Lisboa and 3004-516 Coimbra, Portugal
[28] Affiliated with an Institute or an International Laboratory Participating within the DUNE Collaboration
[29] SLAC National Accelerator Laboratory, Menlo Park, CA 94025, USA
[30] Universidad de Colima, Colima, Mexico
[31] University of Manchester, Manchester M13 9PL, UK
[32] Universidad del Magdalena, Santa Marta, Colombia
[33] University of Texas at Arlington, Arlington, TX 76019, USA
[34] Tel Aviv University, Tel Aviv-Yafo, Israel
[35] University of Sussex, Brighton BN1 9RH, UK
[36] Université Paris-Saclay, CNRS/IN2P3, IJCLab, 91405 Orsay, France
[37] University of Cincinnati, Cincinnati, OH 45221, USA
[38] Taras Shevchenko National University of Kyiv, 01601 Kyiv, Ukraine
[39] Institut de Physique des 2 Infinis de Lyon, 69622 Villeurbanne, France
[40] Indiana University, Bloomington, IN 47405, USA
[41] Pacific Northwest National Laboratory, Richland, WA 99352, USA
[42] University of Warwick, Coventry CV4 7AL, UK
[43] University of California Irvine, Irvine, CA 92697, USA
[44] University of Vigo, E-36310 Vigo, Spain
[45] University of Hyderabad, Gachibowli, Hyderabad 500046, India
[46] York University, Toronto, ON M3J 1P3, Canada
[47] Instituto Superior Técnico—IST, Universidade de Lisboa, 1049-001 Lisboa, Portugal
[48] University of North Dakota, Grand Forks, ND 58202-8357, USA
[49] Universidad de Guanajuato, Guanajuato, C.P. 37000, Mexico
[50] Faculdade de Ciências da Universidade de Lisboa—FCUL, 1749-016 Lisboa, Portugal
[51] Massachusetts Institute of Technology, Cambridge, MA 02139, USA
[52] University College London, London WC1E 6BT, UK
[53] University of Edinburgh, Edinburgh EH8 9YL, UK
[54] Wellesley College, Wellesley, MA 02481, USA
[55] Antalya Bilim University, 07190 Döşemealtı/Antalya, Turkey
[56] Pontificia Universidad Católica del Perú, Lima, Peru
[57] Ohio State University, Columbus, OH 43210, USA
[58] University of Florida, Gainesville, FL 32611-8440, USA
[59] Louisiana State University, Baton Rouge, LA 70803, USA
[60] Daresbury Laboratory, Cheshire WA4 4AD, UK
[61] Istituto Nazionale di Fisica Nucleare Laboratori Nazionali di Pisa, Pisa, PI, Italy
[62] Università di Pisa, I-56127 Pisa, Italy
[63] Istituto Nazionale di Fisica Nucleare Sezione di Catania, I-95123 Catania, Italy
[64] Università di Catania, 2-95131 Catania, Italy
[65] Universidad Nacional de Asunción, San Lorenzo, Paraguay
[66] Colorado State University, Fort Collins, CO 80523, USA
[67] Michigan State University, East Lansing, MI 48824, USA
[68] Istituto Nazionale di Fisica Nucleare Sezione di Lecce, 73100 Lecce, Italy
[69] Università del Salento, 73100 Lecce, Italy
[70] Istituto Nazionale di Fisica Nucleare Sezione di Genova, 16146 Genova, Italy
[71] Istituto Nazionale di Fisica Nucleare Sezione di Bologna, 40127 Bologna, Italy
[72] Università di Bologna, 40127 Bologna, Italy
[73] Universidad EIA, Envigado, Antioquia, Colombia
[74] Queen Mary University of London, London E1 4NS, UK
[75] University of California Davis, Davis, CA 95616, USA
[76] Universidade Federal de Alfenas, Poços de Caldas 37715-400, MG, Brazil
[77] University of Chicago, Chicago, IL 60637, USA
[78] Panjab University, Chandigarh 160014, India
[79] Indian Institute of Technology Guwahati, Guwahati 781039, India
[80] Istituto Nazionale di Fisica Nucleare Laboratori Nazionali del Sud, 95123 Catania, Italy
[81] Beykent University, Istanbul, Turkey
[82] University of Iowa, Iowa City, IA 52242, USA
[83] Lancaster University, Lancaster LA1 4YB, UK
[84] Northern Illinois University, DeKalb, IL 60115, USA
[85] Los Alamos National Laboratory, Los Alamos, NM 87545, USA
[86] IRFU, CEA, Université Paris-Saclay, F-91191 Gif-sur-Yvette, France

[87] Istituto Nazionale di Fisica Nucleare Sezione di Milano Bicocca, 3-I-20126 Milano, Italy
[88] University of Insubria, Via Ravasi, 2, 21100 Varese, Italy
[89] Università di Milano Bicocca, 20126 Milano, Italy
[90] Universidad Católica del Norte, Antofagasta, Chile
[91] University of Birmingham, Birmingham B15 2TT, UK
[92] Indian Institute of Technology Hyderabad, Hyderabad 502285, India
[93] STFC Rutherford Appleton Laboratory, Didcot OX11 0QX, UK
[94] University of Bern, CH-3012 Bern, Switzerland
[95] Wichita State University, Wichita, KS 67260, USA
[96] Oregon State University, Corvallis, OR 97331, USA
[97] University of Bucharest, Bucharest, Romania
[98] University of Pittsburgh, Pittsburgh, PA 15260, USA
[99] Università degli Studi di Genova, Genova, Italy
[100] Virginia Tech, Blacksburg, VA 24060, USA
[101] Istituto Nazionale di Fisica Nucleare Sezione di Napoli, I-80126 Napoli, Italy
[102] Johannes Gutenberg-Universität Mainz, 55122 Mainz, Germany
[103] University of California Santa Barbara, Santa Barbara, CA 93106, USA
[104] University of Wisconsin Madison, Madison, WI 53706, USA
[105] Royal Holloway College London, London TW20 0EX, UK
[106] Universidad Antonio Nariño, Bogotá, Colombia
[107] University of Antioquia, Medellín, Colombia
[108] Universidad Sergio Arboleda, Bogotá 11022, Colombia
[109] Universidad Nacional de Ingeniería, Lima 25, Peru
[110] William and Mary, Williamsburg, VA 23187, USA
[111] Universtà degli Studi di Padova, I-35131 Padova, Italy
[112] Laboratoire de Physique des Deux Infinis Bordeaux—IN2P3, F-33175 Gradignan, Bordeaux, France,
[113] Physical Research Laboratory, Ahmedabad 380009, India
[114] Indian Institute of Technology Kanpur, Uttar Pradesh 208016, India
[115] University of Toronto, Toronto, ON M5S 1A1, Canada
[116] Columbia University, New York, NY 10027, USA
[117] Korea Institute of Science and Technology Information, Daejeon 34141, Republic of Korea
[118] University of Pennsylvania, Philadelphia, PA 19104, USA
[119] Ulsan National Institute of Science and Technology, Ulsan 689-798, Republic of Korea
[120] Southern Methodist University, Dallas, TX 75275, USA
[121] Université Paris Cité, CNRS, Astroparticule et Cosmologie, Paris, France
[122] University Grenoble Alpes, CNRS, Grenoble INP, LPSC-IN2P3, 38000 Grenoble, France
[123] Duke University, Durham, NC 27708, USA
[124] Istituto Nazionale di Fisica Nucleare Sezione di Milano, 20133 Milano, Italy
[125] University of Parma, 43121 Parma, Italy
[126] University of Mississippi, University, MS 38677, USA
[127] University of California Riverside, Riverside, CA 92521, USA
[128] Istituto Nazionale di Fisica Nucleare Laboratori Nazionali di Frascati, Frascati, Roma, Italy
[129] Centro Brasileiro de Pesquisas Físicas, Rio de Janeiro 22290-180, RJ, Brazil
[130] Universidade Federal do Rio de Janeiro, Rio de Janeiro 21941-901, RJ, Brazil
[131] Nikhef National Institute of Subatomic Physics, 1098 XG Amsterdam, The Netherlands
[132] University of Amsterdam, NL-1098 XG Amsterdam, The Netherlands
[133] Northwestern University, Evanston, Il 60208, USA
[134] Valley City State University, Valley City, ND 58072, USA
[135] University of Cambridge, Cambridge CB3 0HE, UK
[136] University of Hawaii, Honolulu, HI 96822, USA
[137] Universidade Federal de São Paulo, São Paulo 09913-030, Brazil
[138] California Institute of Technology, Pasadena, CA 91125, USA
[139] Università degli Studi di Napoli Federico II, 80138 Napoli, Italy
[140] Sapienza University of Rome, 00185 Roma, Italy
[141] Istituto Nazionale di Fisica Nucleare Sezione di Roma, 00185 Roma, Italy
[142] Drexel University, Philadelphia, PA 19104, USA
[143] Iowa State University, Ames, IA 50011, USA
[144] Stony Brook University, SUNY, Stony Brook, NY 11794, USA
[145] Texas A&M University, College Station, TX 77840, USA
[146] University of South Carolina, Columbia, SC 29208, USA
[147] Rutgers University, Piscataway, NJ 08854, USA
[148] University of Sheffield, Sheffield S3 7RH, UK
[149] Istituto Nazionale di Fisica Nucleare Sezione di Padova, 35131 Padova, Italy

[150] Rice University, Houston, TX 77005, USA
[151] Institute for Research in Fundamental Sciences, Tehran, Iran
[152] Madrid Autonoma University and IFT UAM/CSIC, 28049 Madrid, Spain
[153] University of Notre Dame, Notre Dame, IN 46556, USA
[154] Institute of Physics, Czech Academy of Sciences, 182 00 Prague 8, Czech Republic
[155] Syracuse University, Syracuse, NY 13244, USA
[156] Radboud University, NL-6525 AJ Nijmegen, The Netherlands
[157] Czech Technical University, 115 19 Prague 1, Czech Republic
[158] Durham University, Durham DH1 3LE, UK
[159] University of Minnesota Twin Cities, Minneapolis, MN 55455, USA
[160] Tufts University, Medford, MA 02155, USA
[161] Harish-Chandra Research Institute, Jhunsi, Allahabad 211 019, India
[162] University of Granada CAFPE, 18002 Granada, Spain
[163] Boston University, Boston, MA 02215, USA
[164] Occidental College, Los Angeles, CA 90041, USA
[165] South Dakota State University, Brookings, SD 57007, USA
[166] Universidade Federal de Goias, Goiania 74690-900, GO, Brazil
[167] University of Minnesota Duluth, Duluth, MN 55812, USA
[168] Fluminense Federal University, 9 Icaraí Niterói 24220-900, RJ, Brazil
[169] University of California Berkeley, Berkeley, CA 94720, USA
[170] University of Warsaw, 02-093 Warsaw, Poland
[171] University of Puerto Rico, Mayaguez, PR 00681, USA
[172] Chung-Ang University, Seoul 06974, Republic of Korea
[173] Yale University, New Haven, CT 06520, USA
[174] South Dakota School of Mines and Technology, Rapid City, SD 57701, USA
[175] High Energy Accelerator Research Organization (KEK), Ibaraki 305-0801, Japan
[176] Sanford Underground Research Facility, Lead, SD 57754, USA
[177] Dordt University, Sioux Center, IA 51250, USA
[178] Eötvös Loránd University, 1053 Budapest, Hungary
[179] Yerevan Institute for Theoretical Physics and Modeling, Yerevan 0036, Armenia
[180] Abilene Christian University, Abilene, TX 79601, USA
[181] University of Albany, SUNY, Albany, NY 12222, USA
[182] Jackson State University, Jackson, MS 39217, USA
[183] University of Novi Sad, 21102 Novi Sad, Serbia
[184] Erciyes University, Kayseri, Turkey
[185] National Institute of Technology, Kure College, Hiroshima 737-8506, Japan
[186] Florida State University, Tallahassee, FL 32306, USA
[187] University of Texas at Austin, Austin, TX 78712, USA
[188] Università degli Studi di Milano, I-20133 Milano, Italy
[189] Universidade Federal do ABC, Santo André 09210-580, SP, Brazil
[190] Sun Yat-Sen University, Guangzhou 510275, China
[191] Hong Kong University of Science and Technology, Kowloon, Hong Kong, China
[192] Laboratori Nazionali del Gran Sasso, L'Aquila, Italy
[193] Instituto Tecnológico de Aeronáutica, Sao Jose dos Campos, Brazil
[194] Jawaharlal Nehru University, New Delhi 110067, India
[195] University of Athens, 157 84 Zografou, Greece
[196] Istituto Nazionale di Fisica Nucleare Sezione di Pavia, I-27100 Pavia, Italy
[197] Università degli Studi di Pavia, 27100 Pavia, Italy
[198] Centro de Investigación y de Estudios Avanzados del Instituto Politécnico Nacional (Cinvestav), Mexico City, Mexico
[199] Pennsylvania State University, University Park, PA 16802, USA
[200] University of Lucknow, Uttar Pradesh 226007, India
[201] Iwate University, Morioka, Iwate 020-8551, Japan
[202] Comisión Nacional de Investigación y Desarrollo Aeroespacial, Lima, Peru
[203] Centro de Tecnologia da Informacao Renato Archer, Amarais, Campinas CEP 13069-901, SP, Brazil
[204] Gran Sasso Science Institute, L'Aquila, Italy
[205] University of Arizona, Tucson, AZ 85721, USA
[206] Punjab Agricultural University, Ludhiana 141004, India
[207] Jeonbuk National University, Jeonrabuk-do 54896, Republic of Korea
[208] Central University of South Bihar, Gaya 824236, India
[209] Universidad Nacional Mayor de San Marcos, Lima, Peru
[210] Institute of Particle and Nuclear Physics of the Faculty of Mathematics and Physics of the Charles University, 180 00 Prague 8, Czech Republic

[211] University of Michigan, Ann Arbor, MI 48109, USA
[212] National Institute of Science Education and Research (NISER), Odisha 752050, India
[213] Texas AM University - Corpus Christi, Corpus Christi, TX 78412, USA
[214] University of Medellín, Medellín 050026, Colombia
[215] Idaho State University, Pocatello, ID 83209, USA
[216] Jyväskylä University, FI-40014 Jyväskylä, Finland
[217] Kavli Institute for the Physics and Mathematics of the Universe, Kashiwa, Chiba 277-8583, Japan
[218] University of California Los Angeles, Los Angeles, CA 90095, USA
* Correspondence: mastbaum@physics.rutgers.edu
† In memory of our colleague, Dr. Davide Salvatore Porzio, who is no longer with us.

Abstract: The Module-0 Demonstrator is a single-phase 600 kg liquid argon time projection chamber operated as a prototype for the DUNE liquid argon near detector. Based on the ArgonCube design concept, Module-0 features a novel 80k-channel pixelated charge readout and advanced high-coverage photon detection system. In this paper, we present an analysis of an eight-day data set consisting of 25 million cosmic ray events collected in the spring of 2021. We use this sample to demonstrate the imaging performance of the charge and light readout systems as well as the signal correlations between the two. We also report argon purity and detector uniformity measurements and provide comparisons to detector simulations.

Keywords: neutrino; near detector; Deep Underground Neutrino Experiment; DUNE

1. Introduction

Charge readout in liquid argon time projection chambers (LArTPCs) has traditionally been accomplished via a set of projective wire planes, as successfully demonstrated, e.g., in the ICARUS [1], ArgoNeuT [2], MicroBooNE [3], and ProtoDUNE-SP [4,5] experiments, and as planned for the first large detector module of the DUNE experiment currently in preparation at the Sanford Underground Research Facility (SURF) underground laboratory in South Dakota [6]. However, this approach leads to inherent ambiguities in the 3D reconstruction of charge information that present serious challenges for LArTPC-based near detectors, where a high rate of neutrino interactions and an associated high-intensity muon flux cannot be avoided. In particular, 3D reconstruction becomes limited by overlap of charge clusters in one or more projections, and the unique association of deposited charge to single interactions becomes intractable.

To overcome event pile-up, a novel approach has been proposed and is being developed for the LArTPC of the Near Detector (ND) complex of the DUNE experiment, close to the neutrino source at Fermilab. This technology implements three main innovations compared to traditional wire-based LArTPCs: a pixelated charge readout enabling true 3D reconstruction, a high-performance light readout system providing fast and efficient detection of scintillation light, and segmentation into optically isolated regions. By achieving a low signal occupancy in both readout systems, the segmentation enables efficient reconstruction and unambiguous matching of charge and light signals.

This paper describes the first ton-scale prototype of this technology, referred to as Module-0, and its performance as evaluated with a large cosmic ray data set acquired over a period of several days at the University of Bern. Section 2 provides an overview of the detector, as well as of its charge and light readout systems. Section 3 discusses the performance of the charge readout system in detail, and Section 4 does the same for the light readout system. Section 5 then reviews several analyses performed with reconstructed tracks from the cosmic ray data set collected from Module-0 that allow for assessment of the performance of the fully integrated system. Important metrics for successful operation are addressed, such as electron lifetime, electric field uniformity, and the ability to match charge and light signals, among others. Section 6 offers some concluding thoughts.

2. The Module-0 Demonstrator

2.1. Detector Description

The Module-0 demonstrator is the first fully integrated, ton-scale prototype of the DUNE Liquid Argon Near Detector (ND-LAr) design. This detector will consist of a 7×5 array of $1 \times 1 \times 3\,\mathrm{m}^3$ detector modules [7] based on the ArgonCube detector concept [8], each housing two 50 cm-drift TPC volumes with 24.9% optical detector coverage of the interior area. Module-0 has dimensions of $0.7\,\mathrm{m} \times 0.7\,\mathrm{m} \times 1.4\,\mathrm{m}$ and brings together the innovative features of LArPix [9,10] pixelated 3D charge readout, advanced ArCLight [11] and Light Collection Module (LCM) [12] optical detectors, and field shaping provided by a low-profile resistive shell [13]. This integrated prototype also tests the charge and light system control interfaces, data acquisition, triggering, and timing. Module-0 is the first of four functionally identical modules that together will comprise an upcoming 2×2 ND-LAr prototype, known as ProtoDUNE-ND. Following construction and initial tests with cosmic ray event samples, this larger detector will be deployed underground in the NuMI neutrino beam at Fermilab [14] to demonstrate the physics performance of the technology in a similar neutrino beam environment to the DUNE ND. The work presented here describes the analysis of a data set of cosmic ray events obtained with the Module-0 detector, installed in a liquid argon cryostat at the Laboratory for High-Energy Physics of the University of Bern. Over a period of eight days, the detector collected a sample of approximately 25 million self-triggered cosmic ray-induced events along with sets of diagnostic and calibration data. The data collection period included an array of characterization tests and data collection with changes to detector trigger conditions and thresholds and with the TPC drift field as high as 1 kV/cm. For a brief second running period of about three days, the cryostat was emptied and refilled following a series of gas purges rather than complete evacuation in order to assess the purity impact; this is discussed further in Section 5.1. A gallery of events of different types is shown in Figure 1. These images illustrate the rich 3D raw data from the pixelated charge readout system, the imaging capabilities for complex event topologies, and the low noise levels.

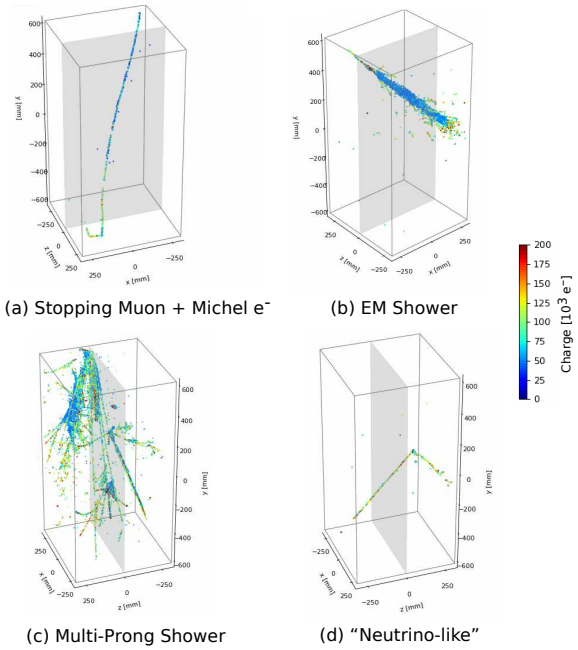

Figure 1. Gallery of four representative cosmic ray-induced events collected with Module-0, as recorded in the raw event data, with the collected charge converted to units of thousands of electrons. In all cases, the central plane in grey denotes the cathode, and the color scale denotes the collected charge. Here, (**a**) shows a stopping muon and the subsequent Michel electron decay, (**b**) denotes an electromagnetic (EM) shower, (**c**) is a multi-prong shower, and (**d**) is "neutrino-like" in that the vertex of this interaction appears to be inside the active volume.

A schematic showing an exploded view of Module-0 with annotations of the key components is provided in Figure 2, and a photograph of the interior of the Module-0 detector as seen from the bottom prior to final assembly is shown in Figure 3. The module is divided into two identical TPC drift regions sharing a central high-voltage cathode that provides the drift electric field. Opposite the cathode at a distance of 30 cm are the anode planes, pixelated with charge-sensitive gold-plated pads where drifting ionization electrons are collected. The sides of the module are covered with photon detectors—alternating ArCLight and LCM tiles. The TPC drift region is surrounded by a resistive field shell made of carbon-loaded Kapton films. This low-profile field cage provides field shaping to ensure a uniform electric field throughout the TPC volumes.

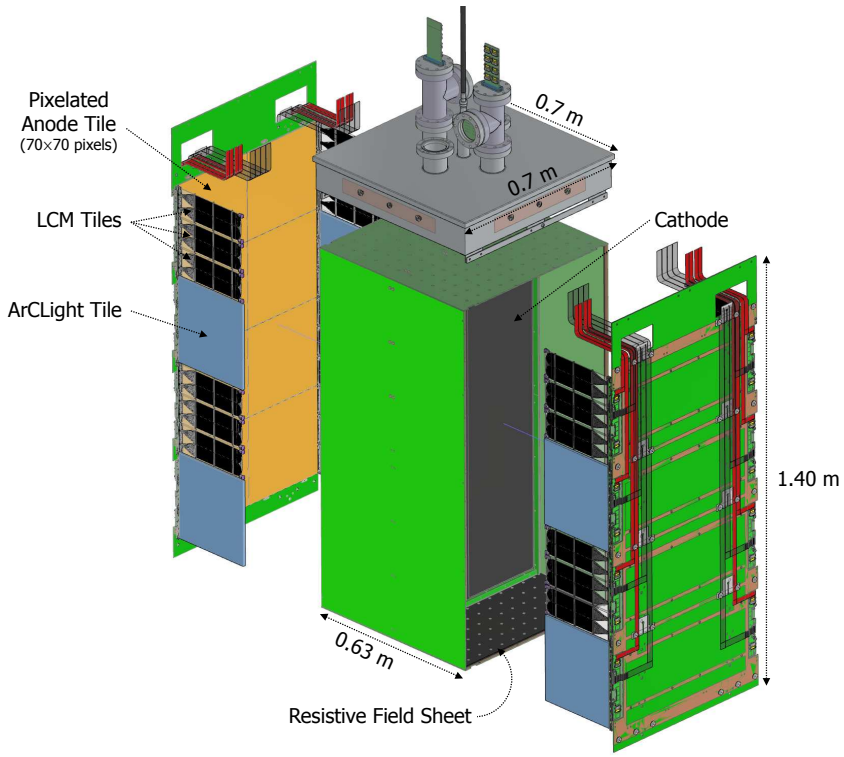

Figure 2. Schematic of the 0.7 m × 0.7 m × 1.4 m Module-0 detector with annotations of the key components.

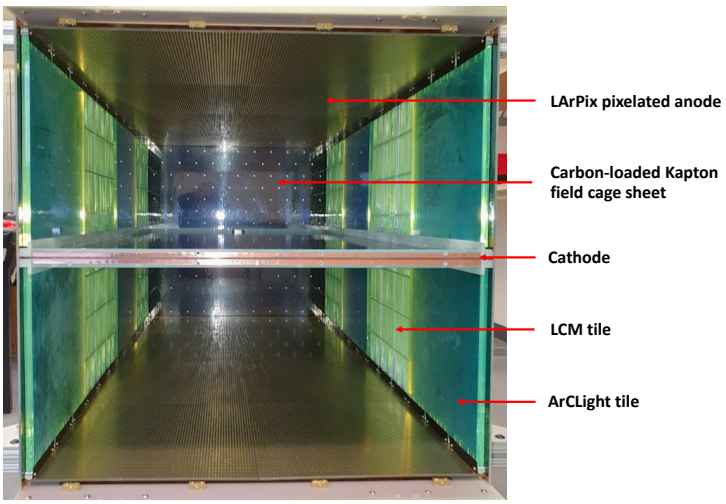

Figure 3. Photograph of the Module-0 detector interior as seen from the bottom with annotations of the key components.

2.2. The Charge Readout System

The charge readout is accomplished using a two-dimensional array of charge-sensitive pads on the two anode planes parallel to the cathode. While pixel-based charge readout has already been implemented in gaseous TPCs, LArTPCs have additional challenges due to restrictions on power dissipation. A proof of principle for pixelated charge readout in a single-phase LArTPC is described in Ref. [15], where a test device was exposed to cosmic ray muons. Readout electronics were also developed [9,16] and successfully applied in a pixel-readout LArTPC. Each of the anode planes on opposite sides of the central cathode is comprised of a 2×4 array of anode tiles. Each tile is a large-area printed circuit board (PCB) containing a 70×70 grid of 4900 charge-sensitive pixel pads with a 4.43 mm pitch. On the back of each PCB is a 10×10 grid of custom low-power, low-noise cryogenic-compatible LArPix-v2 application-specific integrated circuits (ASICs) [10], as shown in Figure 4. Each ASIC is a mixed-signal chip consisting of 64 analog front-end amplifiers, 64 analog-to-digital converters, and a shared digital core that manages configuration and data I/O. Each pixel channel functions as an independent self-triggering detector with nearly 100% uptime and is only unresponsive to charge for 100 ns while the front end resets. The LArPix ASIC leverages the sparsity of LArTPC signals. The chip is in a quiescent mode when not self-triggering on ionization activity higher than $\mathcal{O}(100)$ keV. Thus, it avoids digitization and readout of mostly quiescent data. At liquid argon temperatures, the rate of accumulation of spurious charge (leakage current) is about 500 electrons/s. Each channel periodically resets to discard spurious charge that has collected at the input. In total, Module-0 comprises 78,400 instrumented LArTPC pixels.

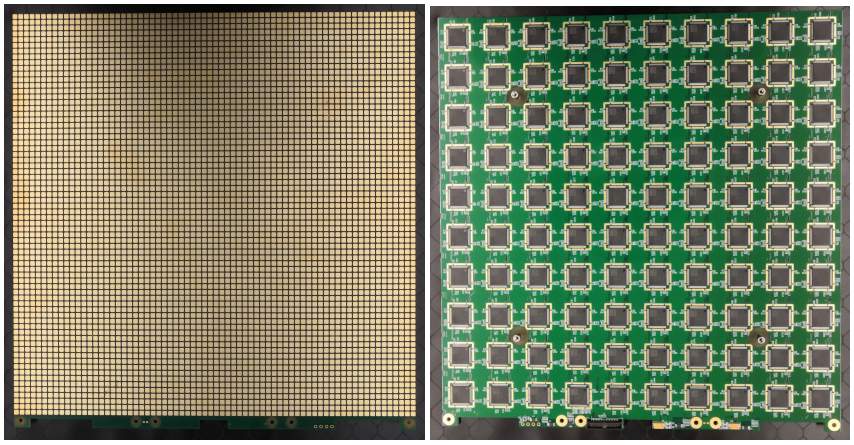

Figure 4. Front (**left**) and back (**right**) of a TPC anode tile. The front contains 4900 charge-sensitive pixels with 4.43 mm pitch that face the cathode, and the back contains a 10×10 array of LArPix ASICs. The dimensions are 31 cm $\times$ 32 cm, with the extra centimeter providing space for the light system attachment points.

Power and data I/O are provided to each tile by a single 34-pin twisted-pair ribbon cable. These cables are connected at the cryostat flange to a custom feedthrough PCB mounted on the cryostat lid. Data acquisition is controlled by the Pixel Array Controller and Network (PACMAN) card (Figure 5), which provides filtered power and noise-isolated data I/O to eight tiles. Two PACMAN controllers are mounted in metal enclosures attached to the outer surface of each feedthrough. During Module-0 operation, the PACMAN controller received a pulse-per-second timing signal for data synchronization between charge readout and light readout systems, and external trigger signals from the light readout system were embedded as markers into the charge readout data stream. Data are carried over a standard copper ethernet cable connected at each PACMAN to a network switch. Subsequently, data are transferred to and from the DAQ system via an optical fiber connection.

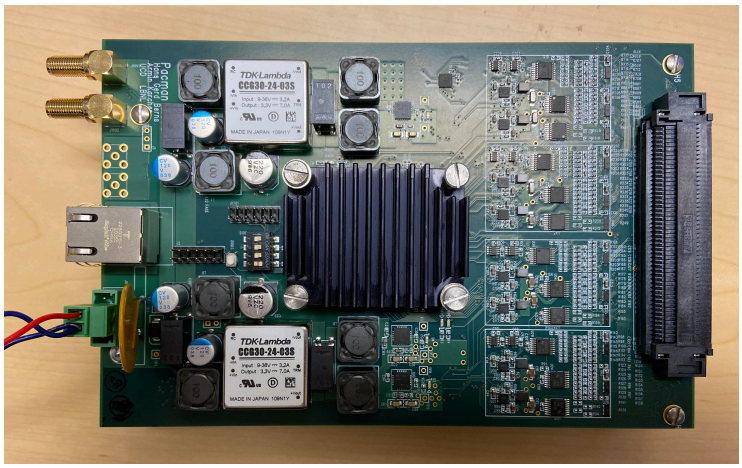

Figure 5. The Pixel Array Controller and Network card (PACMAN), which controls the data acquisition and power for the charge readout system.

For the LArTPC ionization charge measurement, LArPix ASICs mainly operate in self-trigger mode, in which a trigger is initiated on a per-channel basis when a channel-level charge threshold is exceeded. In this mode of operation, LArPix incurs negligible dead time and produces only modest data volumes, due to the sparsity of ionization signals in 3D, even for high-energy events. Serial data packets stream out of the system continuously via the PACMAN boards and are processed offline for analysis. A programmable channel-level threshold is set using internal digital-to-analog converters (DACs), which are tuned so that the spurious (i.e., noise-related) trigger rate is less than 2 Hz for each channel. For Module-0, channel thresholds were operated in two regimes: low and high threshold (see Figure 6). Low-threshold ($\sim$5.8 ke$^-$/pixel or $\sim\frac{1}{4}$ MIP/pixel) operation optimized charge signal sensitivity at the expense of incurring additional triggers due to, e.g., digital pickup, whereas high-threshold ($\sim$10.7 ke$^-$/pixel or $\sim\frac{1}{2}$ MIP/pixel) operation benefited from improved trigger stability at the expense of charge sensitivity. Here, MIP refers to the expected charge deposited by a minimum ionizing particle. Updated revisions of the LArPix ASIC include modifications to the design that reduce pickup and allow channel thresholds to be lowered further. Also, a slight rising trend in event rate can be seen over some of the different periods, most likely due to the emergence during data collection of pixels with a high data rate. It is believed that this small effect, which has no impact on the physics performance, can be mitigated by improving the procedure used to set the thresholds.

ASICs within an anode tile are routed out to the DAQ through a configurable "hydra" network, wherein each ASIC has the ability to pass data packets to and from any adjacent neighbor. The scheme allows for system robustness in the event that an ASIC along the signal path becomes nonfunctional, though none of the 1600 ASICs failed during Module-0 operation. A few-millisecond delay is incurred for data packets produced deeper in the network to reach the PACMAN controller relative to data packets produced closer to it. This is accounted for during hit digitization: Each data packet carries a timestamp at creation when the hit signal is digitized, and when packets reach the PACMAN controller, a receipt timestamp is also assigned. Time ordering and filtering based on packet trigger type is performed offline. In order to monitor the integrity of the data in near-real time, a dedicated nearline monitoring system was developed and operated during the Module-0 run. An automated analysis was performed on each run's raw data once the run ended and provided metrics including system trigger rates, trigger timing and offsets, channel occupancy and trigger rates, and data corruption checks. Cosmic rays produced a self-trigger rate of $\sim$0.25 Hz per pixel. This resulted in a total pixel hit rate of $\sim$20 kHz for the entire Module-0 detector, yielding a modest data rate of 2.5 Mb/s.

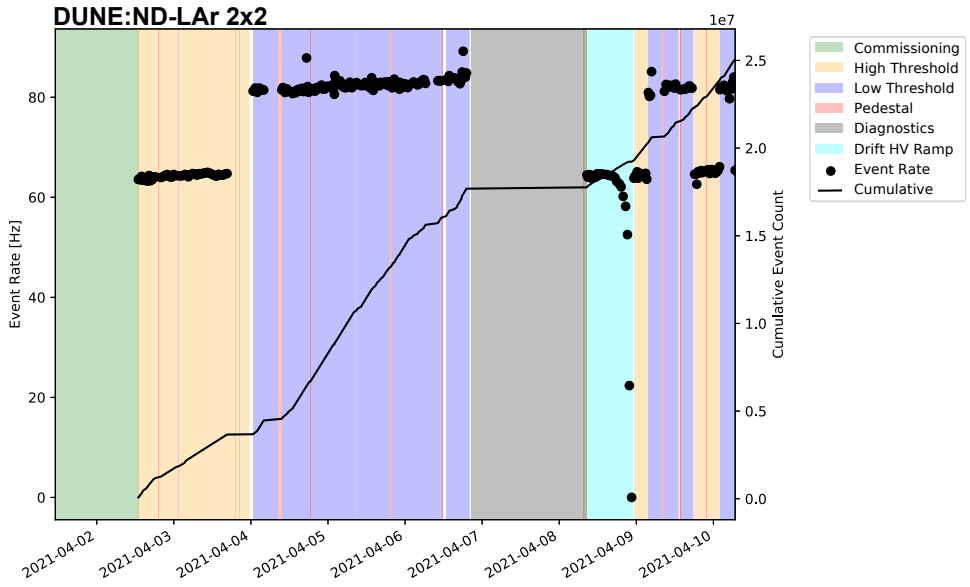

Figure 6. Run event rate and cumulative events as a function of time with respect to charge readout operating condition.

2.3. The Light Readout System

The Light Readout System (LRS) provides fast timing information using the prompt ∼128 nm scintillation light induced by charged particles in LAr. The detection of scintillation photons provides an absolute reference for event timing (t_0) and, when operated in an intense neutrino beam, will allow for the unambiguous association of charge signals from the specific neutrino interactions of interest (i.e., pile-up mitigation). The LRS uses a novel dielectric light detection technique capable of being placed inside the field-shaping structure to increase light yield and localization of light signals. The LRS consists of two functionally similar silicon photomultiplier (SiPM)-based detectors for efficient collection of single UV photons with large surface coverage: the Light Collection Module (LCM) and the ArCLight module. The full LRS system includes these modules together with the ancillary readout, front-end electronics, DAQ (ADCs, synchronization, and trigger), feedthrough flanges, SiPM power supply subsystem, and slow controls, as well as cabling and interconnection between different elements. LCM and ArCLight modules share the same basic operation principle. The vacuum ultraviolet (VUV) scintillation light produced by LAr is shifted from 128 nm to visible light by a wavelength shifter (WLS). Tetraphenyl butadiene (TPB) coated on the surface of the light collection systems provides an efficient WLS, and the emission spectrum of TPB is quite broad, with a peak intensity of around 425 nm (violet light). Part of the light emitted at the surface of the light detection system eventually enters the bulk structure of the detector and is shifted to green light by a dopant (coumarin) in a bulk material, which also acts as a light trap (see Figure 7).

The ArCLight module has been developed by Bern University [11] and uses the ARAPUCA [17] principle of light trapping. The general concept, illustrated in Figure 7 (top), is that violet light enters a bulk WLS volume and is re-emitted as green light, and the volume has a coating reflective to green light on all sides except on the SiPM photosensor window. A dichroic filter transparent to the violet light and reflective for the green is used on the WLS (tetraphenyl butadiene, TPB) side. The overall module dimensions are 300 mm × 300 mm × 10 mm. A photograph of an ArCLight module is shown in Figure 8 (left).

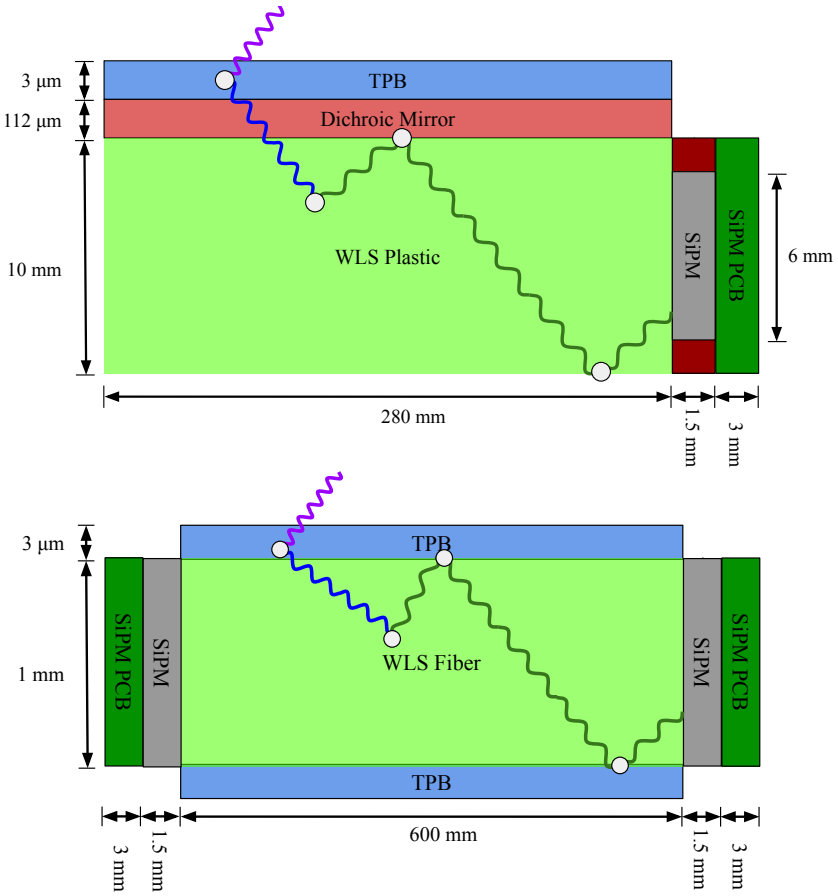

Figure 7. Detection principle of the two types of modules comprising the LRS: a segment of an ArCLight tile (**top**) and a single LCM optical fiber (**bottom**). The wave-like lines indicate example photon trajectories, with the white points indicating interactions. Drawings are not to scale.

The LCM prototype is a frame cantilevered by a PVC plate that holds 25 WLS fibers bent into a bundle, both ends of which are readout by a SiPM light sensor. Fibers are grouped and held by spacer bars with holes fixed on the PVC plate by means of polycarbonate screws to provide matching of thermal contraction. The PVC plate with the WLS fibers is coated with TPB, which re-emits the absorbed VUV light as violet light (∼425 nm). This light is then shifted inside multi-cladding ∅ = 1.2 mm Kuraray Y-11 fibers to green (∼510 nm), and hence, is trapped by total internal reflection guiding it to the SiPM readout at the fiber end, as depicted in Figure 7 (bottom). For each group of LCMs, the center module uses bis-MSB as a WLS rather than TPB to evaluate this alternative option; the photon detection efficiency performance is discussed in Section 4, and the relative performance can be observed in Figure 26. The LCM dimensions are 100 mm × 300 mm × 10 mm. Figure 8 (right) shows three LCMs.

In order to digitize analog signals from SiPMs, a 100 MHz, 10-bit, 64-channel (differential signals, full range ±1.6 V) ADC prototype module in VME standard produced at the Joint Institute for Nuclear Research (JINR) was used (see Figure 9 left). This ADC module streams UDP/TCP data packets via M-link MStream protocol using a 10 Gbps optical link. The ADC boards have the capability to be synchronized via a White Rabbit system [18]. This was not available for the Module-0 run, for which timing synchronization between the charge light systems was provided by a dedicated system shown in Figure 9 (right). To merge data between light and charge systems, a trigger signal generated by the LRS is written out to the charge readout data stream. This trigger signal is also fed to the analog input of both ADCs to allow for precise time matching between ADC boards

for further LRS data analysis. Additionally, a pulse-per-second from a stable GPS source was used for both detection systems to provide accurate synchronization. For the LRS, the pulse-per-second signal was fed to the analog input of each ADC. During the Module-0 run, the LRS operated in a self-triggered mode with adjustable threshold settings. The thresholds for the LCMs are approximately 30 photoelectrons, as discussed in Section 4.

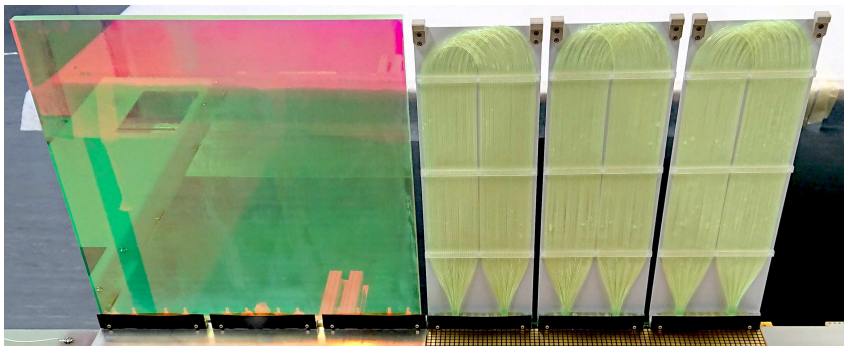

Figure 8. An ArCLight tile (**left**) and three LCM tiles (**right**), as assembled within the Module-0 structure.

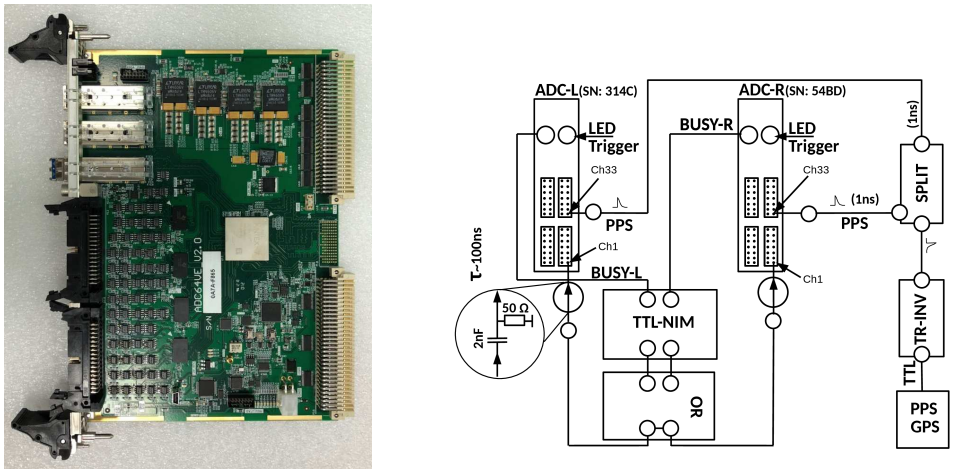

Figure 9. LRS data acquisition components: JINR ADC board (**left**) and synchronization and trigger scheme (**right**).

3. Charge Readout Performance

3.1. System Overview

Module-0 operation represents the first demonstration of the LArPix-v2 pixelated charge readout system in a ton-scale LArTPC. Continuous acquisition and imaging of self-triggered cosmic ray data were successfully exercised, demonstrating the excellent performance of this technology. This section presents an array of studies of the charge readout system performance, including pixel channel signal baselines and time stability, charge response as a function of track position and angle relative to the pixel plane, response uniformity across the instrumented area, ADC saturation, and overall calorimetric measurement performance.

In parallel to this successful series of technological achievements, this first large-scale integrated test highlighted areas for continued improvement in future iterations of the module and ASIC design. This includes improved anode tile grounding and optimization of the pixel pad geometry. In the former case, enhancements to the grounding scheme will enable improved system-wide per-channel charge threshold sensitivity and system trigger stability, specifically allowing for readout of the pixels on the edge of neighboring tiles and mitigating the effects of triggering induced by system synchronization signals observed in the Module-0 data. For the latter case, modifications to the pixel pad geometry are being

explored to decrease the capacitive coupling such that the charge induction response is less pronounced for charges far from the pixel. The aim is to minimize far-field current induction in the pixels, reducing the sensitivity of the readout system to drifting charge that is far from the anode plane. The use of a Frisch grid is a possibility that is also being explored, but none was used during the Module-0 operation, nor is this included in current baseline design. Of the total 78,400 instrumented pixel channels in Module-0, 92.2% were enabled for LArTPC operation. The channels were disabled mainly due to limitations noted above—grounding near tile edges (4.2%), elevated noise levels due to signal pickup (3.1%), high noise or leakage current (0.5%)—and their locations are illustrated in Figure 10. As noted above, no ASICs failed during Module-0 operations.

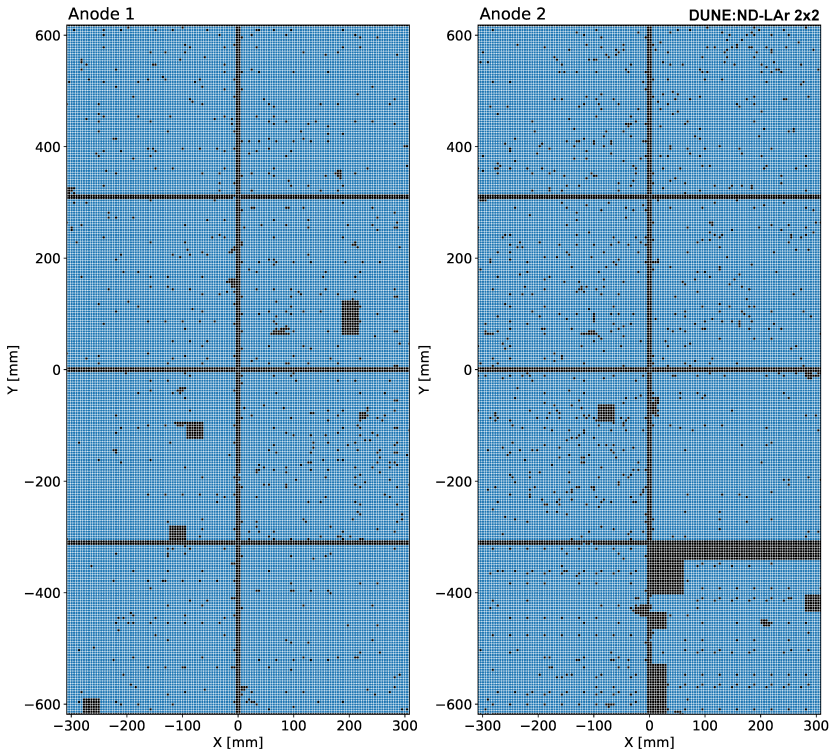

Figure 10. Self-triggered active pixel channels (in blue) and inactive channels (in black). In these coordinates, x is horizontal and y is vertical, both parallel to the anode plane, and z is the drift direction, perpendicular to the anode plane, completing a right-handed system. The origin is the center of the module.

3.2. Noise and Stability

Periodic diagnostics (pedestal) runs were taken to monitor the stability of the charge readout system. These diagnostic runs entailed issuing a periodic trigger on a per-channel basis in a round-robin fashion among channels on a single ASIC. In this way, sub-threshold charge was digitized to monitor channel pedestal and the AC noise stability in time, with the ADC value returned by each digitization reflecting the sum of the quiescent pedestal voltage of the front-end amplifier and the integrated charge. The distributions of ADC values collected during pedestal runs were in agreement with the design expectations, with a median value of ∼78 counts per channel, and pedestal voltage varied by approximately 30 mV between channels. To determine the integrated charge, a correction for this pedestal value must be applied. We computed the channel-by-channel pedestal ADC value by using the truncated mean around the peak of the ADC value distribution of each channel. The signal amplitude in mV was inferred based on the internal reference DAC values and the ASIC analog voltage, and a global gain value of 245 e^-/mV was then used for all channels to convert the signal amplitude to charge.

Additionally, the stability of the charge readout over time was verified using cosmic ray data samples by measuring the most probable value (MPV) and the full width at half maximum (FWHM) of the dQ/dx distribution of MIP tracks for each data run, as shown in Figure 11. To make these track-based measurements, 3D hits registered by the charge system are clustered together using the DBSCAN algorithm [19]. A principal component analysis of hits within each cluster then provides three-dimensional segments that we define as reconstructed tracks. The charge dQ corresponds to the sum of the hits associated with the reconstructed track and the 3D reconstructed track length dx. The dQ/dx distribution is then fitted with a Gaussian-convolved Moyal distribution [20], which is used to extract the MPV and the FWHM. Total system noise contributes ∼950 e^- equivalent noise charge (ENC) to each pixel hit, as assessed using periodic forced triggering of pixel channels in the absence of actual signals (Figure 12). To put this metric in context, the intrinsic energy loss fluctuations associated with the charge from a 4 GeV MIP would be ∼1800 e^- in ND-LAr's 3.7 mm pixel pitch. Therefore, the charge resolution is smaller than the intrinsic physical fluctuations for particle kinematics relevant to ND-LAr.

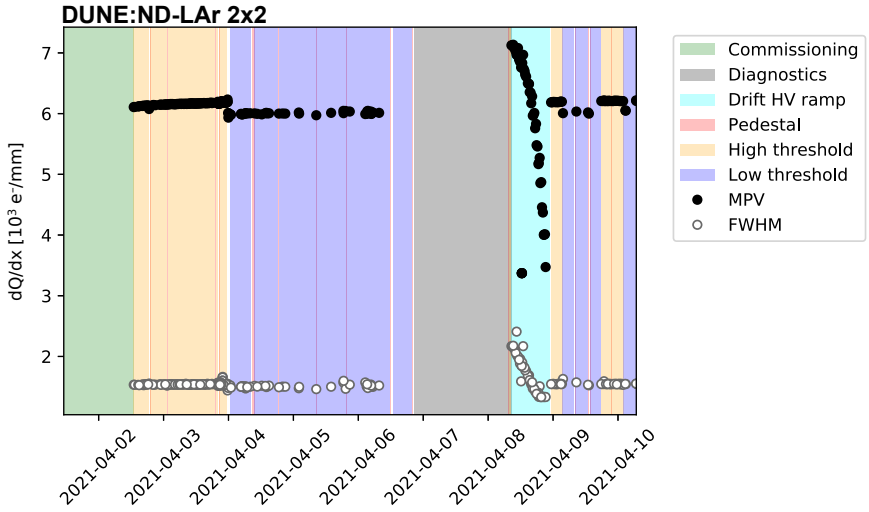

Figure 11. Most probable value (black circles) and full width at half maximum (white circles) of the dQ/dx distribution for each data run. The system shows a good charge readout stability during data taking periods, both for high threshold (yellow bands) and low threshold (purple bands) runs.

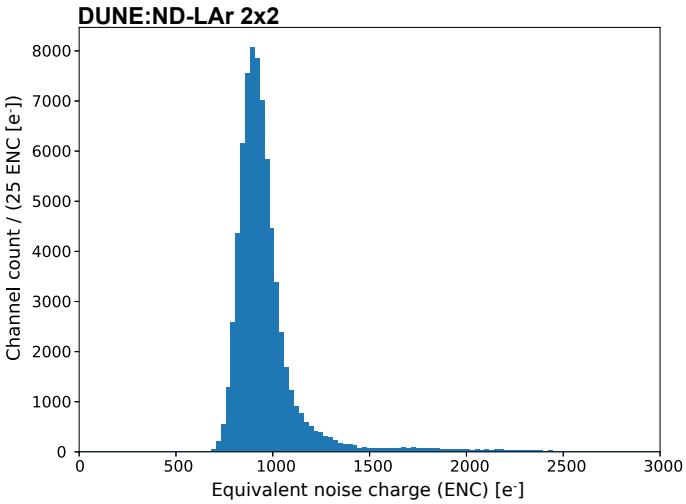

Figure 12. LArPix channel noise in units of electron charge signal as observed using periodic forced triggers. The total system noise is ∼950 e^-, compared to a signal amplitude of ∼1800 e^- for a 4 GeV MIP track in ND-LAr's 3.7 mm pixel pitch.

Examining the corresponding charge in each pixel that has triggered (Figure 13), we identify a sharp rising edge corresponding to the self-trigger threshold at approximately 5.8×10^3 electrons (low threshold) and 11×10^3 electrons (high threshold). Above the self-trigger threshold, a peak at roughly 24×10^3 electrons corresponds to the typical charge deposited by an MIP crossing the full pixel pitch of 4.43 mm. Of note are the markedly different charge distributions of the high- and low-threshold data. We find that for the low-threshold data, the average number of triggers per single channel for MIP energy deposition is substantially larger than for the high-threshold data, with mean values of 1.53 and 1.14, respectively. These numbers are well-reproduced by the Monte Carlo simulation (MC) described in Section 5, with values of 1.52 and 1.12, respectively, for a similar set of reconstructed MIP tracks. Summing the charge of all digitizations on each specific channel for a given event increases the similarity between the low-threshold data and the high-threshold data (Figure 14). This is indicative of a "pre-triggering" effect, in which a channel is triggered by the induced signal generated by the drifting charge in advance of the charge signal arrival at the anode plane, thus motivating the reduction of far-field effects discussed above.

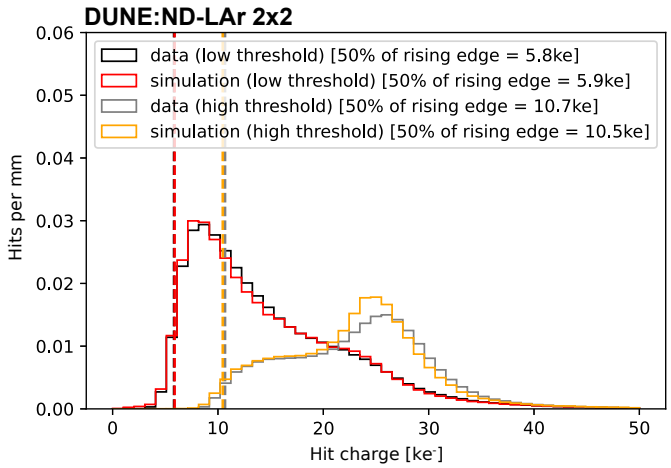

Figure 13. Self-triggered charge distribution for MIP tracks measured in thousands of electrons (ke^-); 50% of the rising edge is shown using vertical lines as indicators of the charge readout self-trigger thresholds. The low- and high-threshold curves were obtained from runs with the same 20 min exposure. Each entry is normalized by hit charge over fitted track length. The MC simulation shown in comparison is described in Section 5.

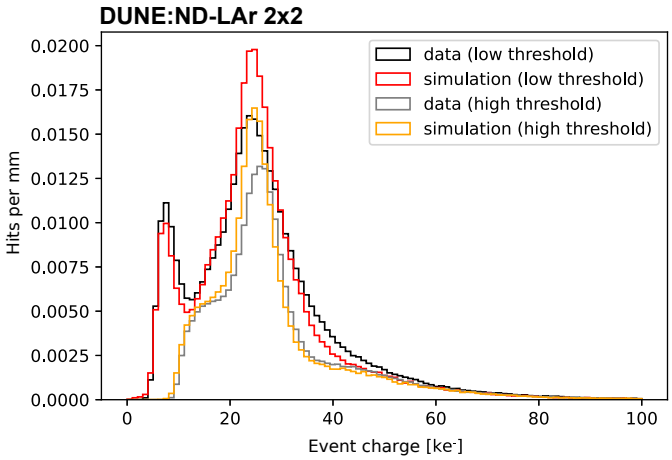

Figure 14. Total event charge per channel for MIP tracks measured in thousands of electrons (ke^-). The MC simulation shown in comparison is described in Section 5.

3.3. Pixel Charge Response

To study the individual pixel charge response, we examine the variation in response based on the track inclination relative to the anode plane (polar angle θ), the orientation angle of the track projected onto the anode plane (azimuthal angle ϕ), and the radial distance from the pixel center to the point of closest approach of the track projected onto the anode plane (r). Figure 15 shows the distribution of these three quantities, normalized by the total track length. Generally, the θ and ϕ distributions are comparable between data and simulations. The r distribution shows significantly more triggers to peripheral tracks than simulated events. An overall normalization difference between high- and low-threshold data reflects the decreased sensitivity to tracks that clip the corners of the pixel.

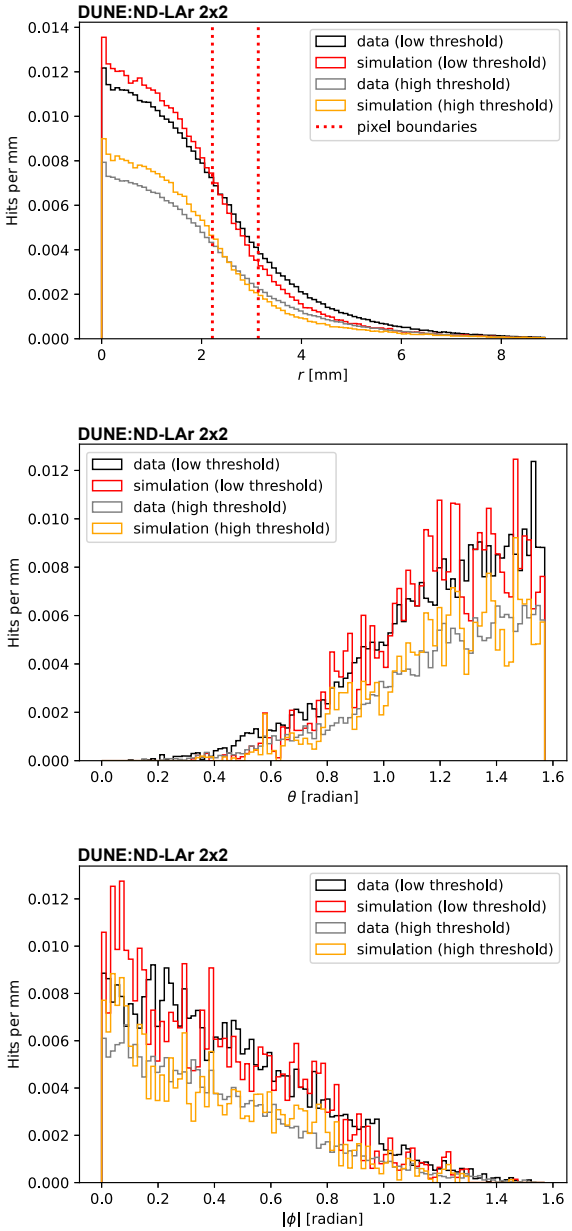

Figure 15. Comparisons of response variation in the radial distance from the pixel center to the point of closest approach of the track projected onto the anode plane (r, **top**), the track inclination relative to the anode plane (polar angle θ, **middle**), and the orientation angle of the track projected onto the anode plane (azimuthal angle ϕ, **bottom**). The MC shown in comparison is described in Section 5.

A similar finding resulted from studying the distance between the MIP ionization axis and the center of the pixel. This ionization axis can be inferred by performing a Hough transform algorithm (HTA) on the x, y, and estimated z dimensions of the hit cloud. A projection of the HTA line onto the pixel plane provides the minimum array of pixels along the axis that could have recorded some charge. This line is then divided into 0.1 mm segments longitudinally. Each individual segment's center then falls into a specific pixel, which is used to determine the distance between the segment center and the pixel center in x and y. The segments are split into three categories: (1) all segments as mentioned above independent of the recorded charge on that particular pixel, (2) those that fell into a pixel which did give a response, and (3) those in pixels that did not trigger. Prior to this categorization, all segments contained by pixels known to be inactive are excluded. In Figure 16, the ratios of the number of segments in the latter two categories to those in the first are shown. The four corners are over-represented for pixels that did not give a response but had the main ionization line crossing their pad. This quantifies the sensitivity of individual pixels to tracks clipping the corners. This difference in sensitivity is characterized by only a 3% drop from pixel center to pixel edge, with the minimum response being 85.5%.

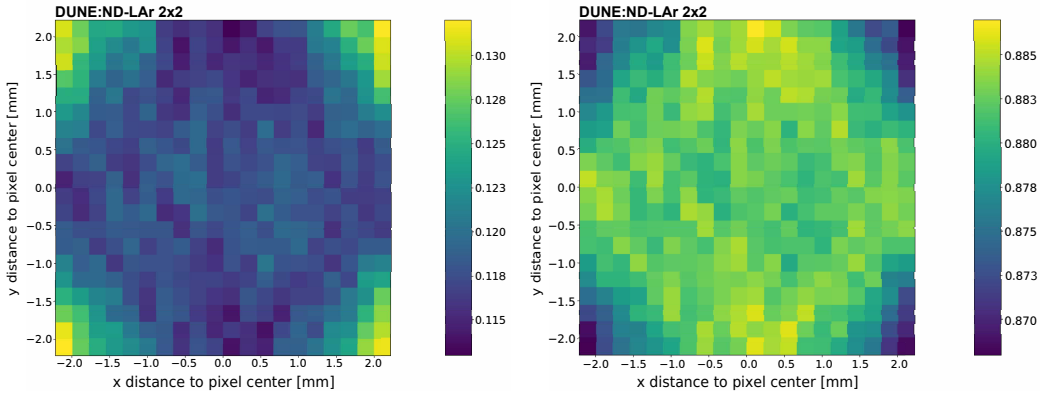

Figure 16. Relative rate of pixel response as a function of the distance between Hough line segments and segment containing pixel's center for pixels on gaps, i.e., no charge response (**left**), and on tracks, i.e., with charge response (**right**) to the total.

Figures 17 and 18 show the charge distribution with respect to the track orientation for low- and high-threshold data, respectively. Overall, similar features appear in each panel: a prominent peak corresponding to the charge deposited by an MIP across a single pixel width. In the r distribution, a secondary distribution of low-charge hits is present, corresponding to tracks that clip the corners of the pixel. This feature is also present in the ϕ distribution as an increase in the spread of the charge as $\phi \to \pi/4$. The θ distribution shows a characteristic increase in the charge as $\theta \to 0$, which corresponds to tracks perpendicular to the anode plane, where each pixel can see a contribution from a relatively long track length. A flattening of the observed charge near $\theta = 0.8$ is a threshold effect and is not present in the low-threshold data. To test the responsiveness of individual pixels and identify potentially malfunctioning channels beyond those known to be inactive, an MIP response map of the entire pixel plane was constructed. This map is the ratio of recorded over expected hits and identifies regions on the pixel plane which are less responsive than others. Both components start off with the same principle of performing an HTA on the x, y, and inferred z dimensions of the hit cloud to obtain the MIP's central ionization axis in 3D. This axis is then projected onto the pixel plane to result in a 2D line. Next, all hits within 8 mm of the line are selected, and the maximum track width is set equal to the most distant point within this radius. To then obtain the first map, all pixels that recorded hits within a radius equal to the maximum track width of the projected line receive an entry. To construct the second map, all existing pixels within that same radius receive an entry. If a pixel is unresponsive, it will not show up in the first but will appear in the second, leading

to a low ratio in that specific area. Selection cuts place requirements on the straightness of tracks relative to the fit Hough lines as well as the consistency with a roughly constant energy deposition profile, and this ensures that the events analyzed consist primarily of MIP-like tracks. Figure 19 shows the resulting MIP response maps for both anode planes.

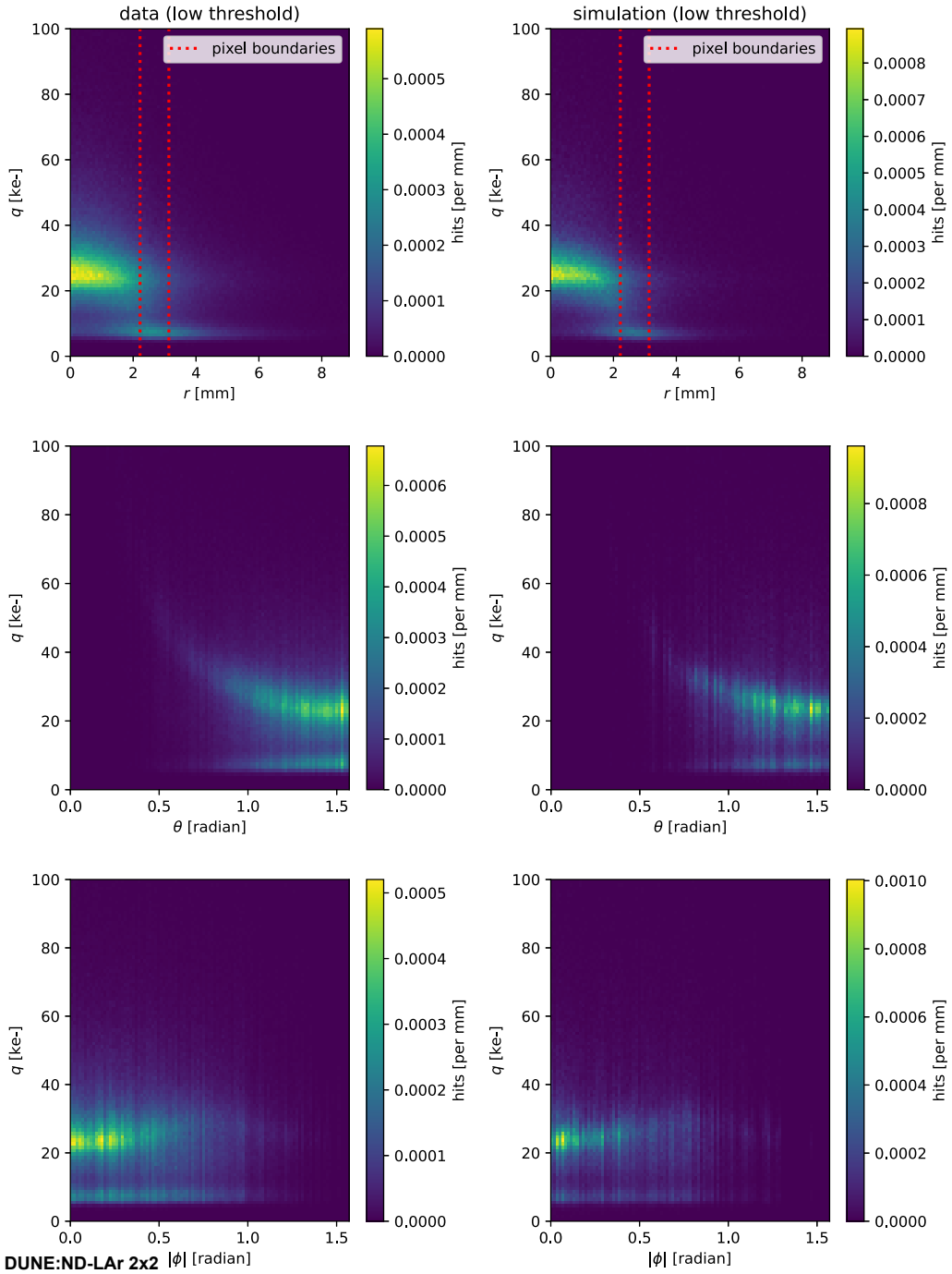

Figure 17. Self-trigger charge distribution for MIP tracks with different track orientations with respect to the pixel, normalized to the number of triggered channels per reconstructed track length. Low-threshold data are used. The MC simulation shown in comparison in the second column is described in Section 5.

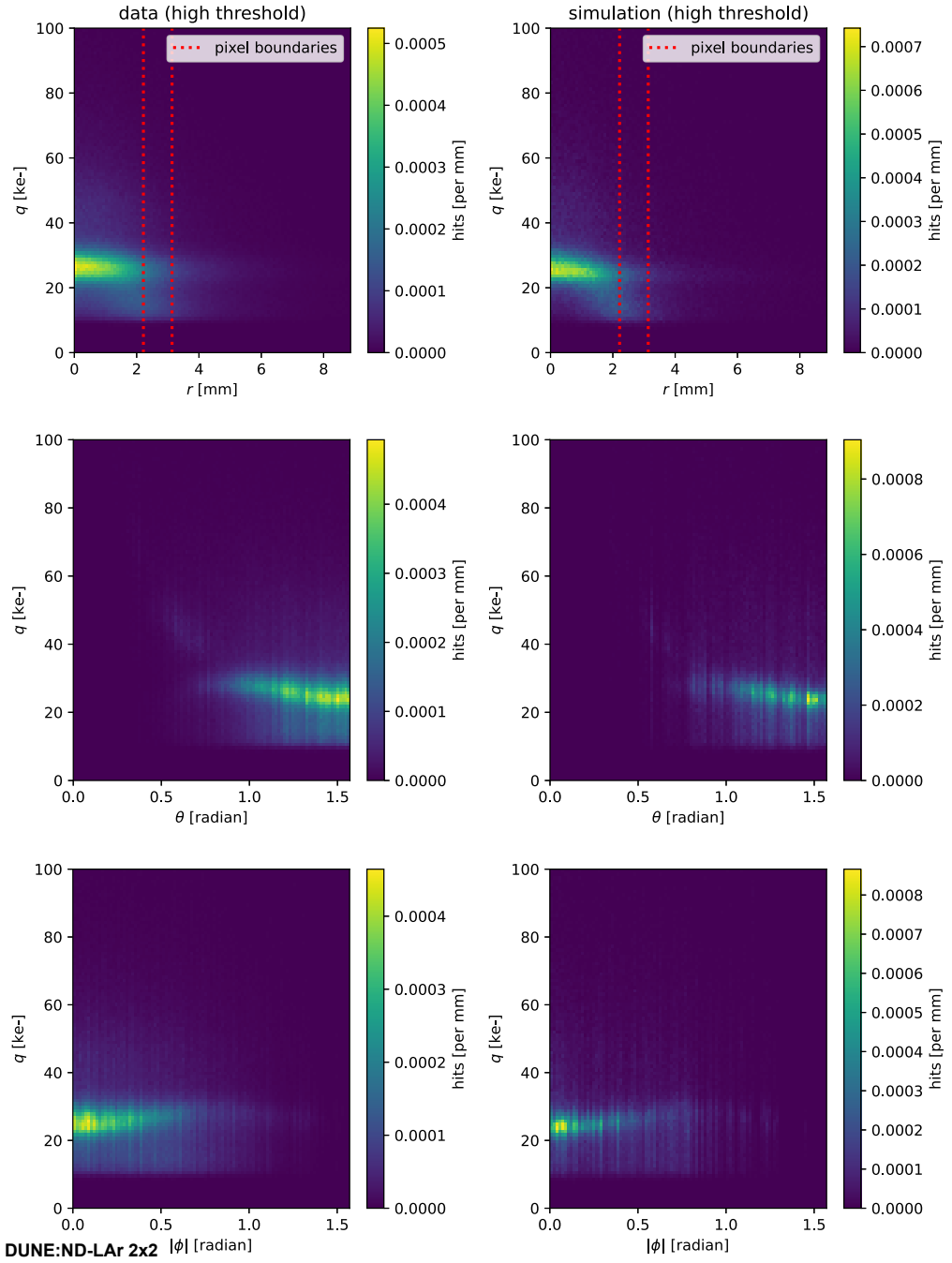

Figure 18. Same as Figure 17 but for high-threshold data.

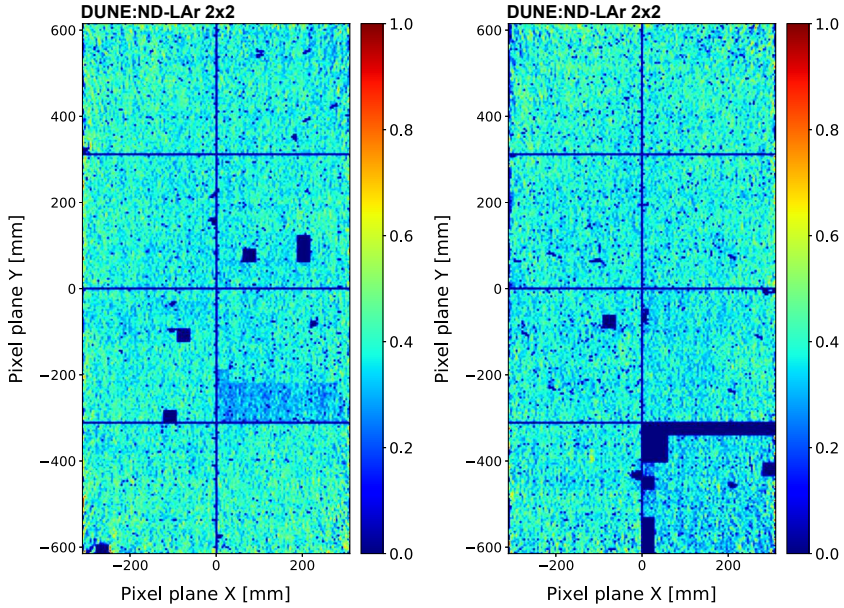

Figure 19. MIP response maps for anode plane 1 (**left**) and anode plane 2 (**right**) showing the fraction of triggered hits on each pixel relative to the expected number based on reconstructed track trajectories.

3.4. Saturation

An additional consideration is saturation in the LArPix-v2 ASIC's 8-bit successive-approximation ADC, which is expected to occur when the charge on a given channel exceeds 200 ke^- within a 2.6 µs time window. A scan for events including saturated packets was performed over eight hours of cosmic ray data acquired at high gain and low threshold. Packets within 1 s of a time synchronization pulse were found to include additional noise and saturation effects, and were excluded. After accounting for this, a small fraction (2.9×10^{-6}) of events with matching charge and light information contained a saturated ADC measurement. These events were manually inspected, and the saturation was clearly uncorrelated in space and time with the physical interactions, but rather, they leaked into the event due to their proximity with a sync pulse. With low thresholds, <0.002% of triggers resulted in ADC saturation, again driven by the pulse-per-second sync signal; channels 35–37 on all chips, which are located physically adjacent to the sync pulse pin, saturated most often and together accounted for 15% of these saturated packets. The ADC count distribution for events with deposited energy between 2 and 10 GeV is shown in Figure 20. These energies are of interest, as they are representative of neutrino interactions at ND-LAr, and the distribution falls well within the dynamic range of the ADC.

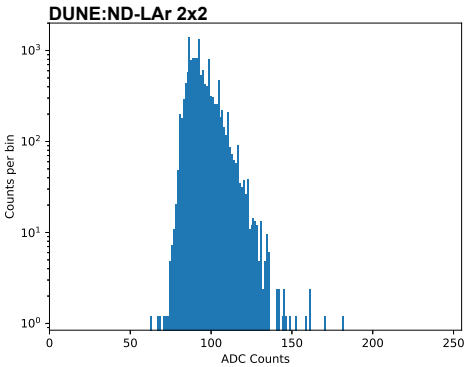

Figure 20. Per-pixel ADC value distribution for cosmic ray events between 2 and 10 GeV. All signals are well within the ADC dynamic range of 0–256 counts.

3.5. Calorimetric Response

Finally, the calorimetric response of the Module-0 charge readout was also studied. Figures 21 and 22 show the variation of the dQ/dx for segments of different lengths relative to the track orientation, defined by the azimuth angle ϕ and the θ angle between the track and a vector normal to the anode plane. The reconstructed tracks used for this analysis come from the low-threshold runs (see Section 1). Events with more than 20 reconstructed tracks were excluded, since they often correspond to large showers or non-cosmic triggers. Tracks were required to be longer than 10 cm and to have at least 20 associated hits. They were then subdivided into segments of variable length from 10 to 400 mm, and the distributions were fit with a Gaussian-convolved Moyal function. The MPV shows a slight dependence on $\cos\theta$, with tracks that impinge perpendicularly to the anode plane tending to have a larger amount of deposited charge per unit length. These data provide insight into subtle effects in the pixel charge response, such as those related to induction effects and electric field uniformity, and enable a data-driven calibration.

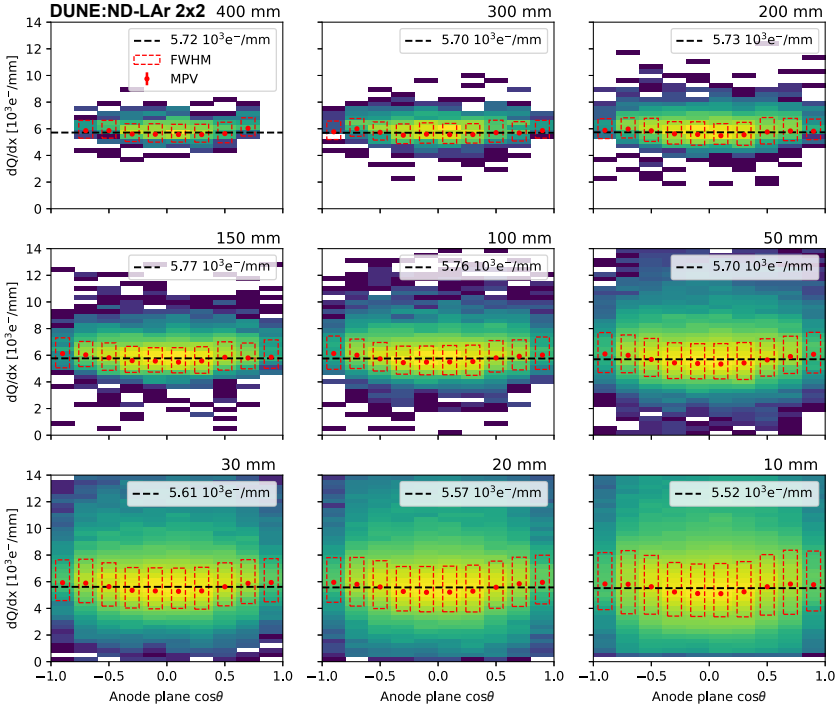

Figure 21. dQ/dx measured for segments of different lengths as a function of the orientation relative to the anode planes. A value of $\cos\theta = 0$ corresponds to segments parallel to the anode plane. The distributions in each bin have been fitted with a Gaussian-convolved Moyal function. The red points correspond to the most probable value of the fitted distribution, and the dashed rectangles correspond to the full width at half maximum. The dashed black line represents the average MPV.

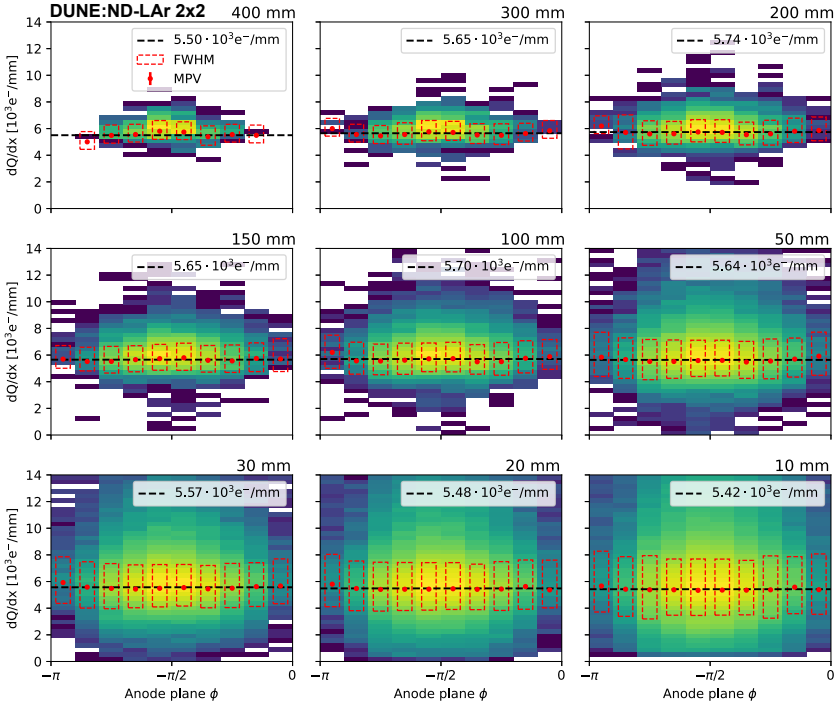

Figure 22. dQ/dx measured for segments of different lengths as a function of the azimuthal angle $\phi = \text{atan2}(y, x)$, where y and x are the components of the segment along the anode plane axes. The distributions in each bin are fitted with a Gaussian-convolved Moyal function. The red points correspond to the most probable value of the fitted distribution and the dashed rectangles correspond to the FWHM. The dashed black line represents the average MPV.

4. Light Readout Performance

4.1. Overview

The Module-0 detector also provided a large-scale, fully integrated test of the light readout system, enabling a detailed performance characterization of the ArCLight and LCM modules, readout, DAQ, triggering, and timing with a large set of events. Using cosmic ray data and dedicated diagnostic runs under a variety of detector configurations, a suite of tests was performed to assess the charge spectrum, inter- and intra-event timing accuracy, and detection efficiency. The subsequent matching of events between the charge and light system is considered in Section 5.3.

4.2. Calibration

Before collecting cosmic data, a SiPM gain calibration was performed using an LED source, where the bias voltage for each SiPM channel was adjusted to obtain a uniform gain distribution across the channels, as shown in Figure 23. The amplification factors for the variable gain amplifiers used in the SiPM readout chain were also tuned and were set to maximum (31 dB), except for LCM channels (21 dB) during cosmic ray data taking, to adjust signals to the input dynamic range of the ADC. LCMs were used to provide an external trigger to the charge readout system, with an effective threshold of about 30 photoelectrons (p.e.). The trigger message, written into the continuous self-triggered data stream of the charge readout system, provides a precise timestamped flag for identifying coincidences between charge and light readout.

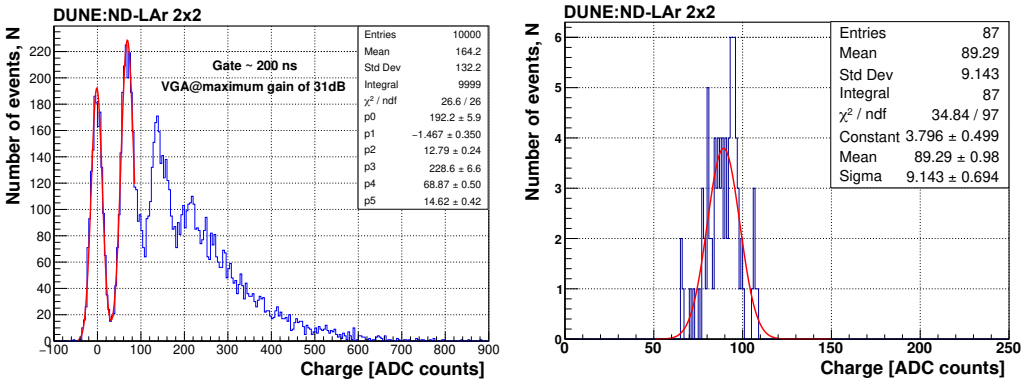

Figure 23. Typical charge spectrum obtained during SiPM gain calibration (**left**); SiPM gain distribution (**right**).

4.3. Time Resolution

Events induced by cosmic muons traversing the TPC volume were used to extract the time resolution of the light detectors. The time measurement proceeds as follows: Each waveform is oversampled through a Fourier transform to increase the number of points on the rising edge, enabling a good linear fit. The sampling of the rising edge was performed over a range from 10% to 90% of the maximum amplitude in order to exclude the region where the behavior is not linear. Then, a linear fit to the baseline is performed, and the crossing point of the rising edge of the signal with the baseline is calculated, providing a robust single-channel event time. This process is illustrated in Figure 24 (left). The extracted time resolution for a pair of neighboring LCM channels is shown in Figure 24 (right) as a function of the signal amplitude. This quantity is obtained by taking the standard deviation of the time difference recorded between the two channels over multiple events without any time-of-flight corrections. For large signals, this resolution approaches ∼2 ns. An example application of the excellent timing resolution for the LCMs is the identification of Michel electrons from stopping muon decays, where the relative timing between the muon and electron signals is dominated by the mean lifetime of the muon, τ ∼2.2 µs. Two examples of signals from a stopping muon and a delayed Michel electron detected by the LCM are shown in Figure 25. Since the muon decay time is variable but follows a well-understood exponential distribution, such events may be used, for example, to study event pile-up in neutrino interactions.

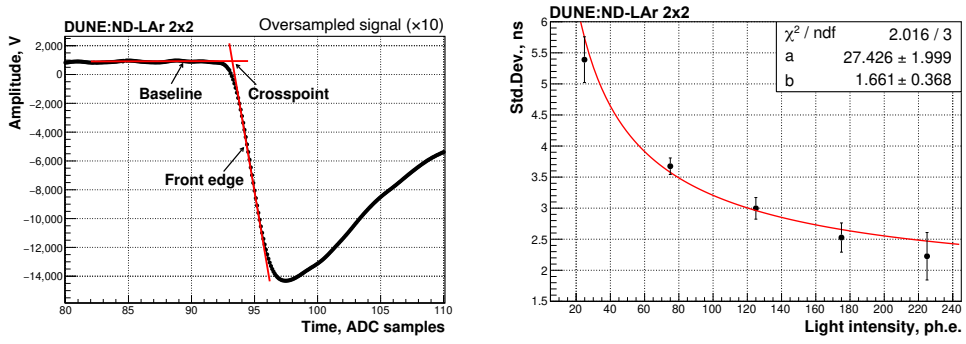

Figure 24. Oversampled signal using Fourier transformation. Red lines show the linear approximations of the rising edge and the baseline (**left**). The time resolution between two LCMs (LCM-011, LCM-017) as a function of the signal response (**right**).

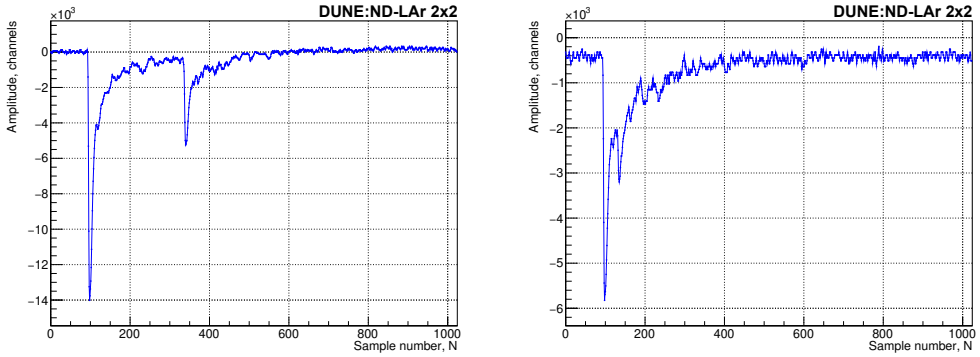

Figure 25. Two examples showing signals of the stopping muon and delayed Michel electron detected by the LCM. The waveforms were digitized at 10 ns intervals.

4.4. Efficiency

To assess the efficiency of the LRS, the scintillation light induced by tracks reconstructed from the TPC charge readout data is used. In particular, cosmic muon tracks crossing the entire detector vertically are considered. In a 3D simulation, the charge of a track is discretized to single points with a 1 mm resolution along the track, assuming an infinitely thin true trajectory. For each point in this voxelized event, the solid angle to the light detector in the detector module is then calculated. Next, assuming isotropic scintillation light emission, the solid angle can be used to compute the geometrical acceptance of the light for each detector tile. The number of photons hitting the detector surface is estimated by multiplying the geometrical acceptance by the number of emitted photons per unit track length and integrating over the full track length. Here, the number of emitted photons per unit track length has been calculated for the nominal electric field strength of 0.5 kV cm^{-1} [21]. Rayleigh scattering, a small effect over the relevant distance scales, is neglected in this calculation.

The overall efficiency of the light detection system can be estimated by comparing the measured number of p.e. and the estimated number of photons hitting the detector surface, as obtained from the simulation described above. Since the waveforms obtained with the light detectors have been integrated using a limited gate length, the actual scintillation light might be underestimated. This was corrected by multiplying the number of reconstructed photons by an integration gate acceptance factor, which is calculated based on the detector response and the scintillation timing characteristics. Figure 26 shows the measured detection efficiency for all ArCLight and LCM modules used in the Module-0 detector. The LCM shows an average efficiency of 0.6%, which enables a light trigger for events depositing MeV-scale energies, with an accurate scintillation amplitude and energy reconstruction. The efficiency of the ArCLight modules is about a factor of 10 lower than the corresponding value obtained with the LCMs, which allows for a larger dynamic range. The ArCLight technology additionally enables a high position sensitivity, which can be used to accurately triangulate the origin of the scintillation light emission point [11]. For the LCM it can be observed that tiles placed at the top (see Figure 26 (right), LCM groups 4–6, 10–12, 16–18, and 22–24) of the TPC show a systematically lower efficiency with respect to tiles placed in the middle of the TPC. This can be explained by an anisotropy of light collection by LCM with respect to the angle of incoming photons, driven by structural non-uniformity of fibers and spaces. The absence of non-uniform effects in the ArCLight tiles due to reflections on the TPC structure or Rayleigh scattering, meanwhile, further indicates that these effects are negligible within the experimental uncertainties. In Module-0, a Hamamatsu MPPC S13360-6025 [22] is used. By replacing the SiPM for future modules with the MPPC S13360-6050 with higher efficiency, the overall PDE would improve by a factor of 1.6 to yield an LCM efficiency of about 1%.

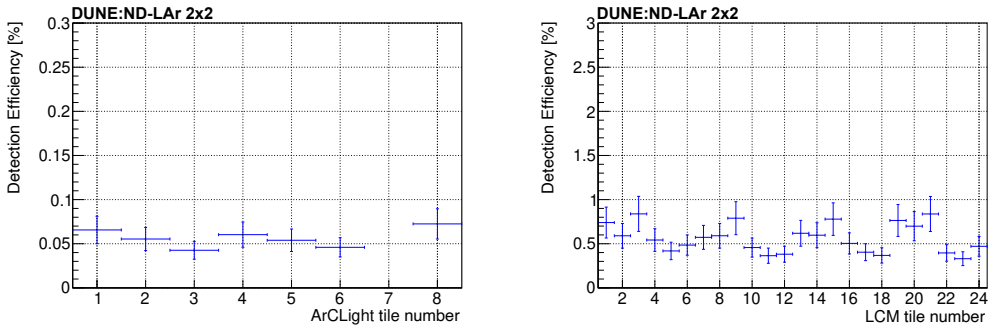

Figure 26. Detection efficiency (as defined in the text) for each ArCLight (**left**) and LCM (**right**) tile (arbitrary numbering). ArCLight tile 7 was disabled during Module-0 data taking. The LCM tiles are placed in sets of three to cover the same area as one ArCLight tile.

5. Measurements with Cosmic Ray Data Samples

The following sections discuss the analyses performed using reconstructed tracks from the large cosmic ray data set collected during the Module-0 run. As discussed in Section 1, the Module-0 detector incorporates several novel technologies for the first time in an LArTPC of this scale. These studies assess the performance of the fully integrated system, including the LArPix charge readout with a very large channel count, the high-coverage hybrid LCM and ArCLight photon detection systems, and their matching; the capability to achieve the necessary levels of LAr purity for physics measurements without prior evacuation of the cryostat; and the degree of drift field uniformity achievable with the low-profile resistive shell field cage. Detailed studies of each of these key detector parameters demonstrate the excellent performance of the integrated system relative to the requirements in view of the operation for the DUNE ND-LAr.

In support of these studies, a sample of cosmic rays has been simulated using CORSIKA [23], a program for the detailed simulation of extended air showers. The passage of the particles through matter was simulated using a Geant4-based Monte Carlo [24]. The detector simulation was performed with larnd-sim [25,26], a set of highly parallelized GPU algorithms for the simulation of pixelated LArTPCs. A track-fitting algorithm was applied to provide an estimate of the particle track angle and location. First, a 3D point cloud was reconstructed using the unique channel index to determine the position transverse to the anode and the drift time. DBSCAN ($k = 5$, $\epsilon = 2.5\,\text{cm}$) [19] was used to find the hit clusters. The cluster radius (ϵ) was tuned using the $k = 5$th-neighbor distance of 3D points from a typical run. Each cluster was then passed through a RANSAC line fit [27] with an outlier radius of $\rho = 8\,\text{mm}$ and 100 random samples. This provided a set of highly collinear points which constitute the reconstructed track.

5.1. Electron Lifetime

The amount of charge collected by the readout system depends heavily on the electron lifetime, τ, in the argon of the TPC volume. The electron lifetime parameterizes (in units of time) how much charge is lost due to attachment to electronegative impurities in the argon, such as oxygen or water, during the drift of the deposited ionization charge toward the anode. The charge measured at the anode, Q, is given by

$$Q = e^{-t/\tau} \cdot R \cdot Q_0, \tag{1}$$

where Q_0 is the amount of the primary ionization charge deposited by a particle in the liquid argon, R is the recombination factor that describes the fraction of charge that survives prompt recombination of the ionization with argon ions prior to drift, and t is the drift time from the point of original charge deposition to detection in the anode plane. Measuring signals originating across the entire TPC via the charge readout system requires a sufficient

electron lifetime in the detector. For the DUNE ND-LAr detector, this requirement is >0.5 ms at a drift electric field of 500 V/cm; this relatively low value compared to other large LArTPC detectors [4,28,29] is due to the relatively short maximum drift length of DUNE ND-LAr (∼50 cm) and allows ND-LAr to meet the charge attenuation performance of the far detector, which specifies a 3 ms lifetime in a detector with a 3.5 m drift length at a 500 V/cm drift field [30]. A measurement of the electron lifetime with Module-0 has been carried out to confirm that the materials used in the detector, which will be similar to those of DUNE ND-LAr, are compatible with the argon purity requirement. Additionally, tracking this parameter as a function of time is necessary to provide a calibration of charge scale for other measurements carried out using the Module-0 charge data.

As seen in Equation (1), charge measurements at the anode depend both on the electron lifetime and the recombination factor. However, by measuring Q as a function of the drift time for a collection of cosmic muon tracks that span the entire drift distance, the dependence on R, which is independent of drift time, can be ignored as an overall normalization factor. Additionally, a more fitting quantity to use in this study is dQ/dx, the measured charge per unit length along the cosmic muon track, given the dependence of the amount of charge seen by a single pixel channel on the orientation of each track. The electron lifetime for each Module-0 data run at a drift electric field of 500 V/cm is measured by applying an exponential fit to the mean dQ/dx of muon track segments as a function of drift time to the anode, assuming a uniform dQ/dx, as illustrated in Figure 27. A sample of anode–cathode-crossing tracks is used for this measurement; these tracks span the entire drift distance, and the absolute drift time associated with each part of the track is known for this track sample. The electron lifetime values measured in Module-0 were consistently above 2 ms for the duration of the run, thus satisfying the $\tau > 0.5$ ms requirement. This trend continued in the second run (Run 2) of Module-0, where cryogenic operations differed from those in Run 1. Run 1 achieved LAr purity through cryostat evacuation before cooldown and LAr filling, while Run 2 made use of a piston purge procedure (repeatedly purging the volume with clean gas), as this is the anticipated approach for the full-scale cryostat of ND-LAr. A recirculation system with filtration was operational during both runs. The filtration was performed in the liquid phase by circulating the LAr through an activated copper getter (Research Catalysts, Inc., Willis, TX, USA, Q-5 Copper Catalyst) and a molecular sieve. The turn around time for the entire argon volume was approximately 2 h. This is similar to other large-scale LArTPC neutrino detectors. Results are shown in Figure 28.

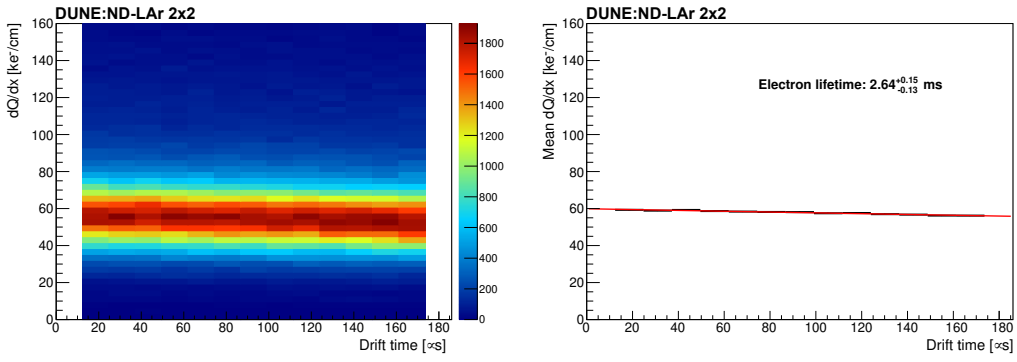

Figure 27. Measured dQ/dx versus drift time for ionization associated with anode-cathode-crossing muon tracks (**left**); mean dQ/dx versus drift time, along with exponential fit, for the same track sample (**right**).

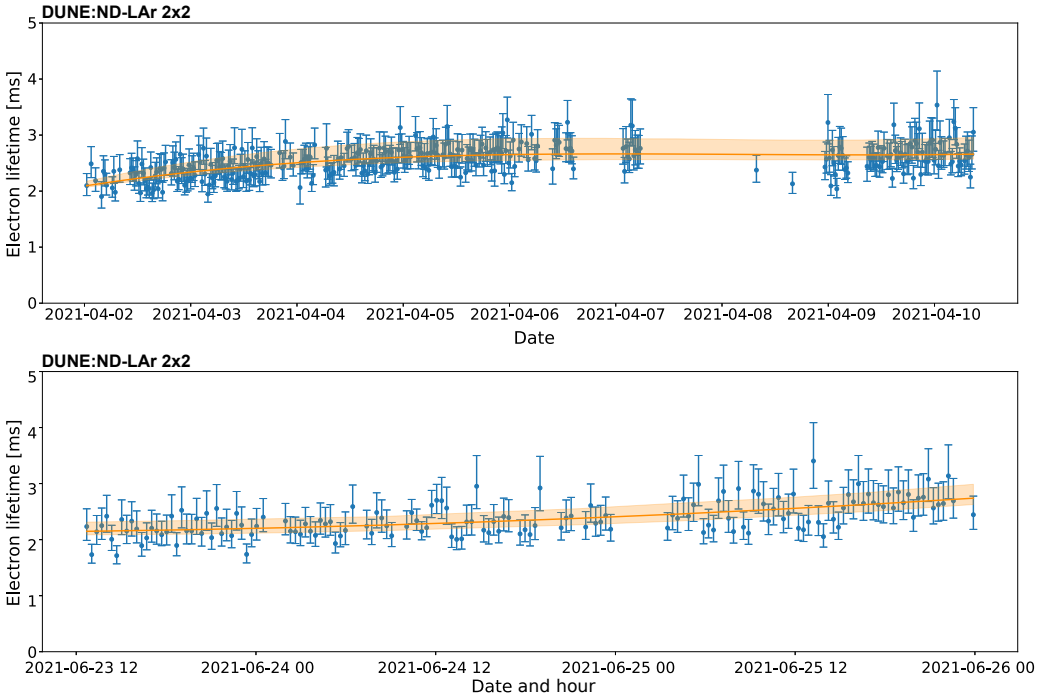

Figure 28. Extracted electron lifetime as a function of time during Module-0 Run 1 (**top**) and Run 2 (**bottom**), with the average uniformly exceeding 2 ms in both cases.

5.2. Electric Field Uniformity

The magnitude of electric field distortions due to space charge effects for Module-0 are expected to be much smaller than other, larger LArTPC detectors running near the surface, such as MicroBooNE [31] and ProtoDUNE-SP [4]. This is due to the relatively small maximum drift length of ∼30 cm of Module-0, compared to ∼2.5 m for MicroBooNE and ∼3.6 m for ProtoDUNE-SP. Even for a maximum drift length of ∼50 cm that is anticipated for DUNE ND-LAr, the impact from space charge effects is expected to be negligible; the fact that ND-LAr will operate 65 m underground will reduce this effect further due to the smaller flux of cosmic muons. However, it is possible that electric field inhomogeneities may arise in the Module-0 detector from other sources. In particular, it is important to determine whether or not the field cage design causes significant distortions of the electric field, which can alter the trajectories ionization electrons take while drifting to the anode plane. Such distortions could lead to incorrect reconstruction of the true position of original energy depositions in the detector due to primary particles ionizing the argon, consequently impacting their trajectory and energy reconstruction. Furthermore, associated modification to the electric field strength throughout the detector can lead to significant impact on the amount of electron–ion recombination experienced by ionization electrons, leading to bias in reconstructed particle energy scale or degradation of reconstructed particle energy resolution. The use of the novel resistive field cage technology in Module-0, as is anticipated for DUNE ND-LAr, provides an important opportunity to study the impact on electric field homogeneity.

Following the methodology developed by the MicroBooNE experiment for the analysis of space charge effects [31], electric field distortions are probed using end points of through-going cosmic muon tracks in Module-0 data. Tracks passing through an anode plane and another face of the detector that is not the other anode plane are selected for this study, providing a known absolute drift time associated with each part of the track via subtracting the time associated with the anode side of the track. The track end point associated with the non-anode side of the anode-crossing track is then probed by measuring the transverse (i.e., perpendicular to the drift direction) displacement from the edge of the TPC active volume, as measured from the y value (TPC top and bottom) or x value (TPC front and back sides,

perpendicular to the drift direction) of the pixel channels at the edge of the detector. The average transverse displacement is recorded as a function of the two directions within the TPC face for all four non-anode faces of the Module-0 TPC. If there are no electric field distortions in the detector, there would be no inward migration of ionization electrons during drift, leading to zero transverse displacement of ionization charge with respect to the TPC face for this sample of through-going muon tracks (contamination from stopping muons is expected to be less than 1%). The result of the average transverse displacement measurement is shown for the TPC top and bottom in Figure 29 and for the TPC front and back in Figure 30. A few features not associated with electric field distortions in the detector should be pointed out. First, there are gaps in coverage near the anode planes (z values of roughly $\pm$30 cm) due to a requirement in the track selection that the non-anode side of the track is at least 5 cm away from both anode planes, and near the pixel plane edges (edges of the TPC face) due to a requirement that the non-anode side of the track is not located within 1 cm (2 cm) of these features. These selection criteria were introduced to minimize contamination of the sample from poorly reconstructed muon tracks. Some residual contamination is seen near the edges of the pixel planes where the measured average transverse spatial offset is artificially large due to edge channels of the pixel planes being turned off for data collection, leading to the ends of tracks being clipped off near the edges of pixel planes. Second, the two horizontal bands in the bottom-right corner of the right side of Figure 30 are associated with a known grounding issue of an ArCLight unit in this part of the detector. The vertical gap in the right panel of Figure 29 is due to inactive channels in this region of the anode plane (see Figure 10).

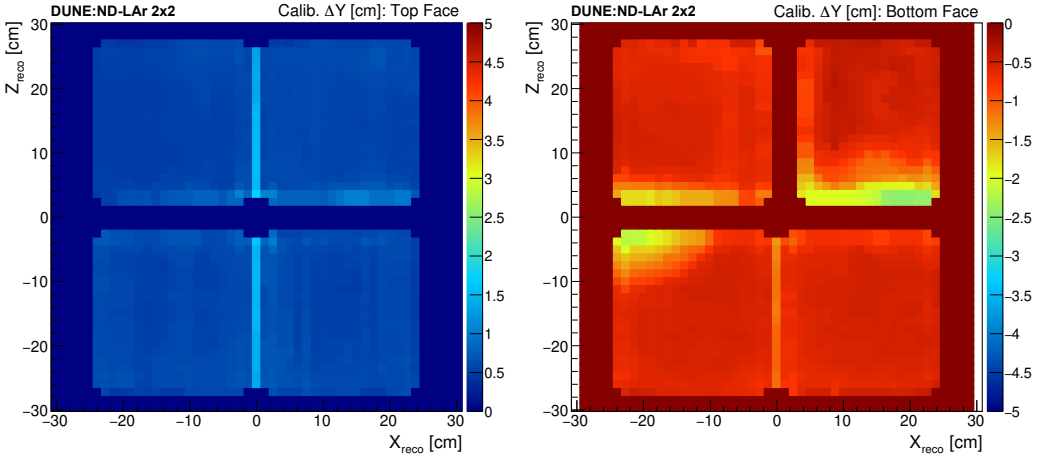

Figure 29. Average spatial offsets (ΔY) measured at the top (**left**) and bottom (**right**) of the Module-0 detector. These offsets in cm indicated by the color scale are measured with respect to the location of the pixel channels at the edge of the detector.

After accounting for these two artifacts, non-negligible transverse spatial offsets are observed near the cathode (central horizontal lines in Figure 29, central vertical lines in Figure 30), roughly 1 cm on average but as large as 2.5 cm in some places in the TPC. After adding an additional $\sim$1 cm to these measurements to account for the separation between the edge pixel channels and the field cage (or light detectors in the case of the front and back of the TPC), the average (maximum) transverse spatial offset experienced by drifting ionization charge originating near the cathode is roughly 2 cm (3.5 cm). Ascribing this transverse drift to an additional electric field component strictly in the direction transverse to the TPC faces, the average (maximum) transverse electric field magnitude leading to this amount of inward drift of ionization charge is roughly 30 V/cm (60 V/cm). The associated average (maximum) impact to the electric field magnitude in the detector is 0.2% (0.7%). This is below the conservative physics requirement of 1% maximum allowed deviation of the electric field magnitude within 95% of the detector volume, indicating that the design of the field cage is adequate for the physics goals of DUNE ND-LAr. It is worth

pointing out that this physics requirement for electric field distortions corresponds to after detector calibrations have been carried out, while the measurements presented here have no calibration applied. It is thus expected that the calibrated electric field map would be even more homogeneous at DUNE ND-LAr. An additional study is carried out to determine whether the small electric field distortions in the Module-0 detector vary substantially over time. A substantial time dependence of the electric field distortions may complicate efforts to obtain a calibrated electric field map in the DUNE ND-LAr detector using cosmic muons, neutrino-induced muons, or dedicated calibration hardware. Average transverse spatial offsets were measured at four different places on each side of the Module-0 cathode as a function of time, spanning two full days of data collection. The results of the study are shown in Figure 31. No substantial time dependence of transverse spatial offsets is observed (<0.2 cm), indicating that calibration of the underlying electric field distortions is achievable by averaging the measured spatial offsets over at least a few days of data collection. A study of electric field stability over longer periods of time is planned in future prototyping of the DUNE ND-LAr detector concept.

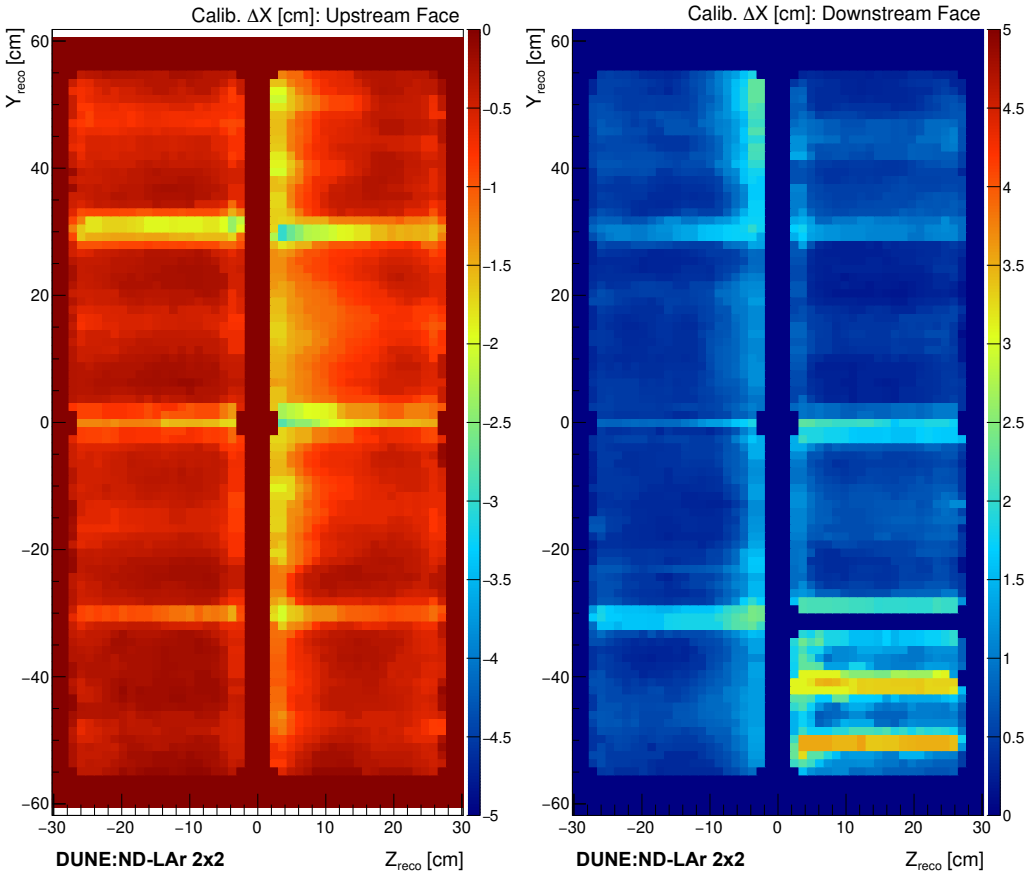

Figure 30. Average spatial offsets (ΔX) measured at the front (**left**) and back (**right**) of the Module-0 detector. These offsets in cm indicated by the color scale are measured with respect to the location of the pixel channels at the edge of the detector.

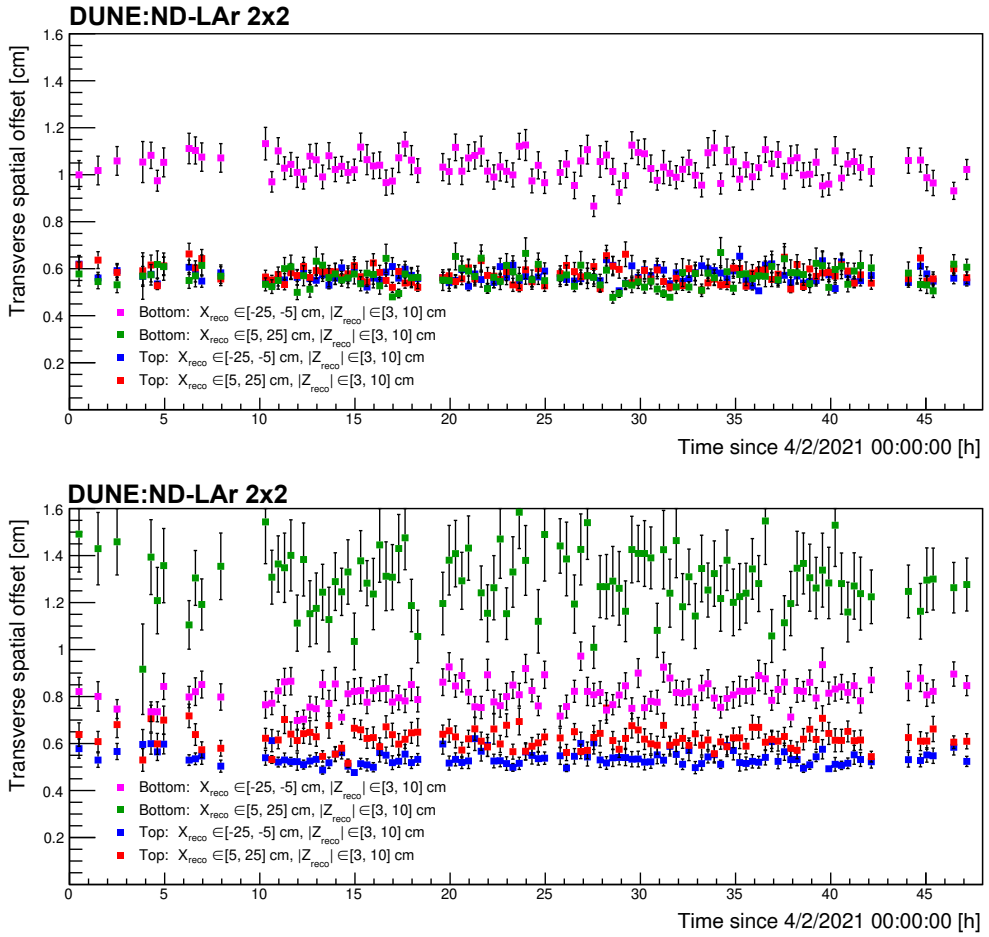

Figure 31. Time dependence of spatial offsets in the $-z$ (**top**) and $+z$ (**bottom**) drift volumes. These offsets are measured with respect to the location of the pixel channels at the edge of the detector.

5.3. Charge–Light Matching

Efficient matching between signals in the charge and light readout systems is essential, as this enables the use of light to disambiguate pile-up of separate neutrino interactions within a single beam spill. The unique association between charge and light signals is a nontrivial problem in a large-volume LArTPC, especially in an environment with a high rate of neutrino event pile-up, such as DUNE ND-LAr. This motivates the modular design, in which the full active volume is composed of an array of optically isolated TPC volumes, each with high coverage of optical detectors with fast timing and good spatial resolution. Charge–light matching in Module-0 has been accomplished via association with precision GPS-synchronized timestamps in the two systems. Here, two performance metrics are considered: the efficiency of matching for a selection of tracks as a function of the allowed coincidence time window and the resolution in terms of the offset between the two systems' timestamps. Figure 32 shows the matching efficiency for varying definitions of the allowed time window for coincidence formation for a selection of anode–cathode-crossing muon tracks. The overwhelming majority of these are single tracks, as the cosmic ray activity is predominantly track-like and the probability of having another event in the same $\sim$200 µs window is very small. For conservative matching parameters of around $\pm$5 µs, an efficiency of $\geq$99.7% is found. In this study, the timing resolution is limited by the spatial resolution of the tracking from the charge readout, not by the intrinsic light detector timing resolution, which is discussed in Section 4. Next, Figure 33 illustrates the relative time offset between the two systems for the Module-0 prototype, again for a selection of anode–cathode-crossing tracks. The distribution exhibits a Gaussian core and a tail. The asymmetric tail of the distribution, captured by a Crystal Ball fit [32–34], is due to track

truncation near the boundaries of the pixel planes. The Gaussian component of the Crystal Ball fit is also shown; the standard deviation of the Gaussian, 0.4 µs, is identified as the charge readout timing resolution. The physics requirements for ND-LAr require that the resolution in the drift dimension be at least as precise as that across the anode plane, i.e., the pixel pitch divided by $\sqrt{12}$, or 1.3 mm. The resolution extracted in Module-0 corresponds to 0.6 mm at a drift electric field of 500 V/cm, thus meeting the requirement.

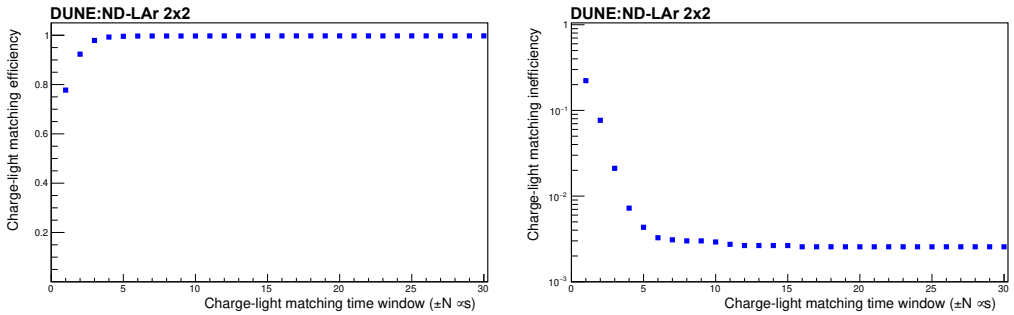

Figure 32. Charge–light matching efficiency in linear scale (**left**) and inefficiency in logarithmic scale (**right**) for light detector triggers matched to charge readout triggers for anode–cathode-crossing tracks. The time window corresponds to the time difference between the external trigger on the charge readout (t_0) and the light detector trigger time.

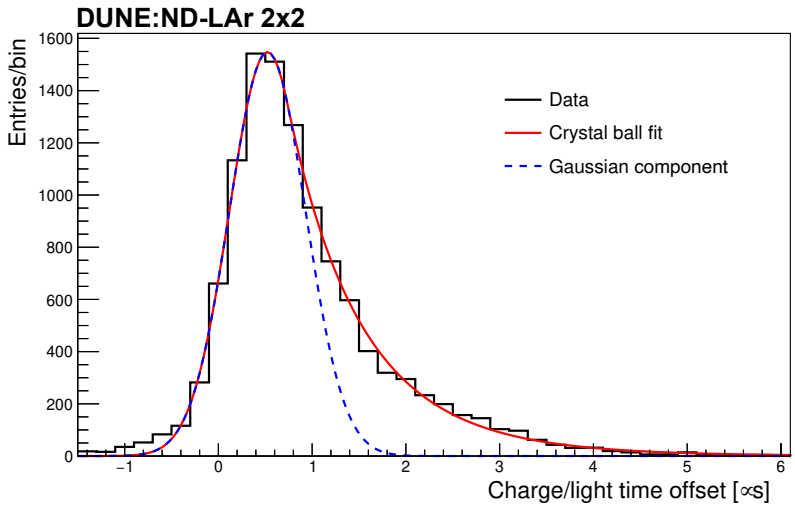

Figure 33. Distribution of time differences between the external trigger on the charge readout (t_0) and the time of the light detector event for anode–cathode-crossing tracks.

5.4. Correlation of the Charge and Light Yield

Matched charge and light events as shown in Figure 34 provide another data sample which may be used to study the correlation between the relative charge and light yields in the detector. These yields are related to electric field-dependent recombination effects.

To describe the recombination mechanism in LAr, we formalize the ionization and excitation states generated by the deposited energy of a traversing particle as follows:

$$N_i + N_{ex} = QY + LY, \tag{2}$$

where the sum of available ionization (N_i) and excitation (N_{ex}) states determines the total number of electrons (QY) and photons (LY) generated in LAr. The number of ionization states N_i is given by

$$N_i = \frac{E_{dep}}{W_i}, \; W_i = 23.6\,\text{eV}, \tag{3}$$

where W_i is the ionization work function [35], and E_{dep} is the deposited energy. In the absence of charge attenuation and impurities, the total charge Q arriving at the anode depends only on the initially produced ionization charge $Q_0 = N_i e$ as

$$QY = N_i \cdot R_c, \tag{4}$$

$$LY = N_i \left(1 + \frac{N_{ex}}{N_i} - R_c\right), \tag{5}$$

where the charge recombination factor R_c is dependent on the electric field ϵ, and e is the electron charge. In the presence of impurities, the electron lifetime correction is applied first; see Equaiton (1). Increasing ϵ leads to less recombination between argon ions and ionization electrons, and thus, more free charge carriers are present in the TPC drift field, increasing the total detected charge at the anode plane. At the same time, a reduced charge recombination factor corresponds to less scintillation light produced within the TPC, leading to a decrease of the light yield at higher electric fields, as expressed by Equation (4). Hence, the amount of charge yield and the amount of light yield observed in the detector are expected to be negatively correlated. To describe the recombination of electron–ion pairs, we focus on the most commonly used models, namely the Box [36] and Birks models [37], and compare the results of Module-0 measurements with those of the ICARUS [38] and ArgoNeuT [39] experiments. The Box model assumes zero electron diffusion, zero ion mobility, and a uniform distribution of ionization electrons produced within a 3D box along the path of the ionizing particle. The collected charge Q is given by

$$Q = Q_0 \cdot \frac{A_{\text{Box}}}{\xi} \cdot \ln(\xi), \tag{6}$$

where Q_0 denotes the primary ionization charge, and ξ is

$$\xi = \frac{N_0 K_r}{4a^2 \mu \epsilon}, \tag{7}$$

where a is the linear size of the charge 'box', N_0 denotes the number of electrons in the box, and K_r is the recombination rate constant. μ and ϵ define the electron mobility and the electric field, respectively. Note that in the limit of an infinite electric field ϵ, the collected charge at the anode plane corresponds to the initially produced charge, Q_0. The Birks model describes the collected charge QY as

$$QY = N_i \cdot \frac{A_{\text{Birks}}}{1 + \frac{k_B}{\epsilon} \cdot \frac{dE}{dx}} = \frac{Q_0}{e} R_c, \tag{8}$$

where A_{Birks} and k_B are fitting constants. In this formulation of the Birks model, for infinite electric field intensities $\epsilon \to \infty$, the recombination factor does not go to 1 and is limited to $R_c \to A$. We can now express the light yield as

$$LY = N_i \left(1 + \frac{N_{ex}}{N_i} - \frac{A_{\text{Birks}}}{1 + \frac{k_B}{\epsilon} \cdot \frac{dE}{dx}}\right). \tag{9}$$

However, since the fraction of excited states $\frac{N_{ex}}{N_i}$ is not precisely known, the commonly used model for the description of the light yield in scintillating materials uses the following formulation:

$$LY = L_0(1 - \alpha R_c) = L_0 R_L, \tag{10}$$

$$L_0 = \frac{E_{dep}}{W_L}, W_L = 19.5\,\text{eV}, \tag{11}$$

where L_0 denotes the number of scintillation photons at zero electric field strength, α is a constant fitted to the data, and W_L is the scintillation work function [40]. This formulation is used in this analysis to evaluate the parameters in the Birks model for the light yield.

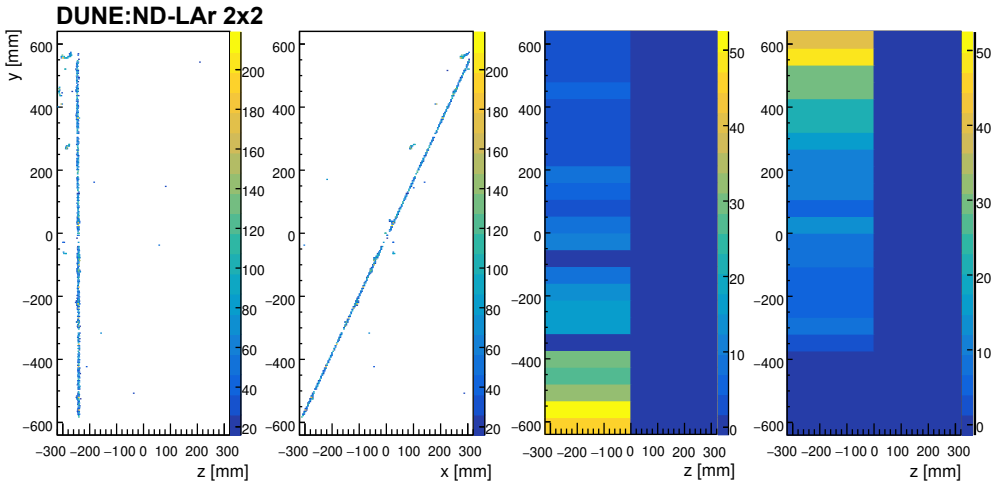

Figure 34. Charge–light matched event display of a cosmic muon track. The left two panels show the TPC charge readout in a z–y projection (**left**) and x–y projection (**center left**). The right two panels show the light detector responses for the arrays at $-x$ (**center right**) and $+x$ (**right**), with each bin along the vertical axis representing the strength of signal read by individual SiPMs.

To study the charge and light correlation in Module-0, data samples at different electric field intensities ranging from 0.05 kV cm^{-1} to 1.00 kV cm^{-1} were acquired and analyzed. These events contain information about the collected charge and scintillation light. A selection of vertical through-going tracks, as expected from MIP muons, was used to extract the collected charge and light per unit length of the track. For the measurement of the collected charge per unit track length, the track was divided into 2 cm segments, and the total charge collected from each segment was divided by the segment length. Then, the light yield per unit track length was extracted as

$$\frac{dL}{dx} = \frac{L_{\text{detected}}}{\int \Omega dl \times \text{PDE} \times G}. \tag{12}$$

The factors in this expression include the geometrical acceptance $\int \Omega dl$, the readout gate acceptance G, and the overall PDE of each tile reported in Section 4. The geometrical acceptance was computed based on the charge data and the track segment position with respect to a light detection tile, integrated over the track length. The readout gate acceptance is an estimation of the fraction of photons which reach the SiPM within the readout integration gate of 500 ns. The gate acceptance was measured using the average waveform of the light signals in Module-0 data and was found to be ∼64% for both the LCM and ArCLight modules.

The dQ/dx and dL/dx distributions are well-described by a Landau-convolved Gaussian function, which is used to extract the most probable value (MPV). We note that the fits are performed on raw data, i.e., without additional calibration of the track dE/dx. Due to uncorrected charge losses, the extracted MPV values for charge measurements should be compared with an effective value of ∼1.8 MeV/cm, while MPVs reflective of light measurements correspond to an effective dE/dx ∼2.1 MeV/cm. The dependence of the charge yield and the light yield MPV values with respect to the electric field density is illustrated in Figure 35.

The charge yield and light yield data points were fitted separately to the Birks model, with results shown in Figure 35 and Table 1. We note that for the light yield fit (Figure 35, right), per Equation (10), the A_{Birks} and α_{light} parameters are totally correlated and cannot

be extracted independently. The left panel of Figure 35 also shows a comparison of the charge yield data (red points) to fits calculated using a Birks model (red curve) and Box model (green curve) alongside the results from the ICARUS experiment (blue curve), demonstrating good agreement between the results.

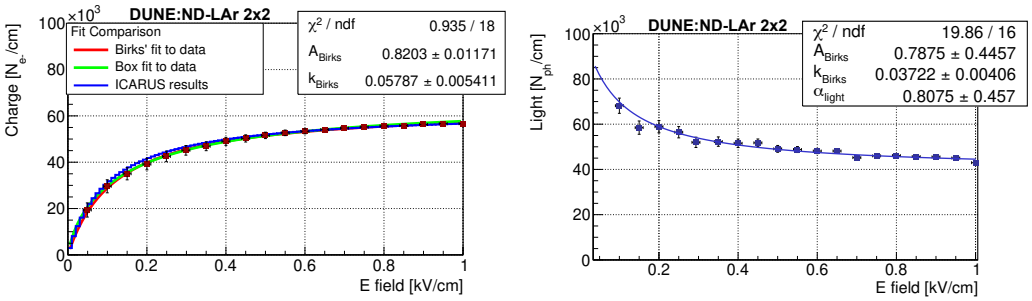

Figure 35. Charge yield as a function of the electric field strength fitted with the Box and Birks models and compared to ICARUS results (**left**). Light yield as a function of the electric field strength fitted separately with the Birks model (**right**).

Table 1. The fitted parameters of the Birks model using the Module-0 data.

Fit Parameters	A_{Birks} [kV g cm^{-3} MeV^{-1}]	k_{Birks} [kV g cm^{-3} MeV^{-1}]
Charge only fit	0.820(11)	0.058(5)
Light only fit	0.79(45)	0.037(4)
Combined fit	0.794(8)	0.045(3)

Next, a combined fit of the Birks model to both charge and light yield data sets was performed. Figure 36 shows the final result of the correlation study. The best fit results for the Birks model parameters are $A_{Birks} = 0.794 \pm 0.008$ and $k_{Birks} = 0.045 \pm 0.003$, with a χ^2/ndf of 23.2/35, with the number of degrees of freedom calculated based on 19 fit points per data set (charge and light) included in the fit and three fit parameters.

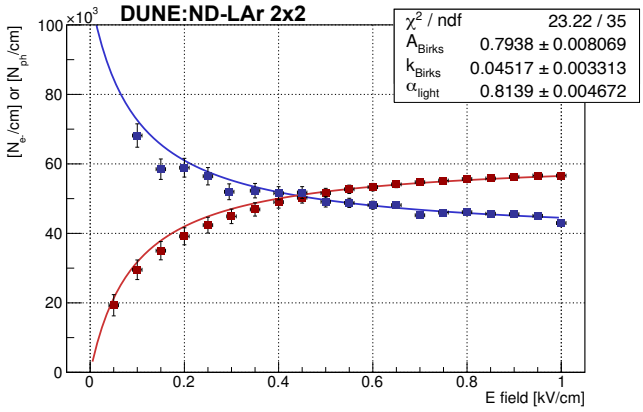

Figure 36. Light yield (blue) and charge yield (red) extracted from a simultaneous fit calculated with the Birks model.

Table 2 summarizes the Birks model parameters obtained with the Module-0 detector and compares them with the parameters found in the ICARUS and ArgoNeuT experiments. The results of the simultaneous fit of the Birks model to the light and charge distributions show reasonable agreement with previous experiments.

Table 2. Comparison of the ICARUS and ArgoNeuT results with those of the current study.

Experiment	A_{Birks} [kV g cm^{-3} MeV^{-1}]	k_{Birks} [kV g cm^{-3} MeV^{-1}]	Reference
ICARUS	0.800(3)	0.0486(6)	[38]
ArgoNeuT	0.806(10)	0.052(1)	[39]
Module-0	0.794(8)	0.045(3)	This work

5.5. Michel Electrons

Michel electrons, i.e., electrons from stopped muon decay, constitute a readily available and versatile tool for the study and characterization of the performance of an LArTPC. They are abundant for surface-level detectors exposed to a large cosmic ray muon flux, and with $\mu \rightarrow e\overline{\nu}_e\nu_\mu$ as the almost exclusive decay channel, the number of events is given by the probability of the muon coming to rest in the detector. The electrons produced by the decay have a well-characterized energy spectrum with a cutoff at ∼50 MeV, and their topology is relatively easy to tag: a long muon track ending with a Bragg peak followed by a short ionization track from the electron at a different angle with respect to the muon direction. Figure 1 includes one example of a stopping muon decaying with a Michel electron in Module-0. The effective muon lifetime of ∼2 µs is short relative to the TPC drift speed, leading to minimal displacement of the muon track endpoint and electron track start. However, it is large relative to the time resolution of the light readout system, allowing the two signals to be tagged separately; the first light pulse corresponding to the muon ionization and the second to the electron, can be easily separated for a large majority of events due to the excellent timing resolution of ArCLight and LCM detectors. Figure 37 shows the event display of a selected Michel electron candidate, with the two peaks showing the waveforms of the light detectors located in one of the two half-TPCs.

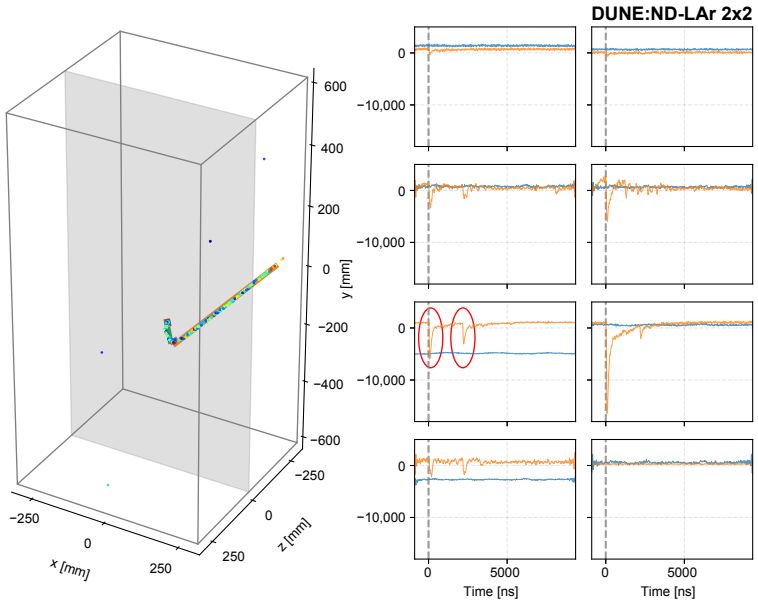

Figure 37. Event display of a Michel electron candidate shown in a 3D view (**left**) and with associated waveforms from photon detectors (**right**). In the right panel, orange and blue indicate the two optically isolated semi-TPCs. The red circles highlight an example in which the two pulses on the photon detectors correspond to the entering muon and the electron resulting from its decay.

The Michel electron candidates' topologies are mainly characterized by a long ionization trail left over by the crossing muon. An automatic selection algorithm based on the event topology and the presence of the Bragg peak at the end of the muon track was developed and applied to the subset of cosmic data. Visual event validation was performed on selected events to validate the analysis. The final distribution of the reconstructed Michel

electron energy based on the automated charge reconstruction is shown in Figure 38. The end point is near the expected true end point of 53 MeV. The spectrum peaks at lower energies mainly as a consequence of partial containment, imperfect clustering, and charge below threshold, particularly from electrons Compton-scattered by Bremmstrahlung photons radiated from the primary electron [41–43].

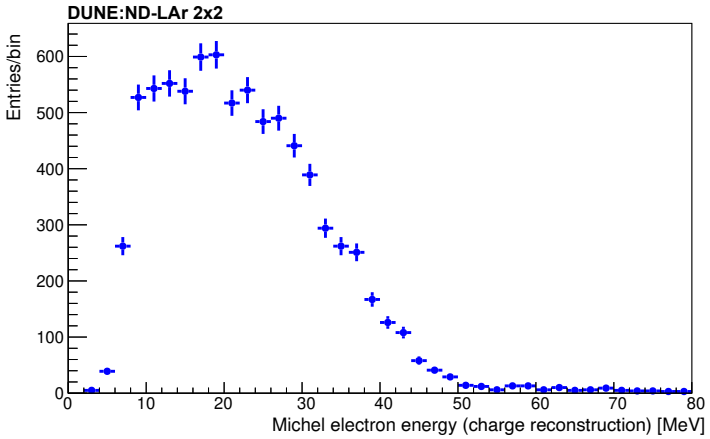

Figure 38. Charge-based energy spectrum of Michel electron candidates from a sample of reconstructed muon decays using the full data set and automated event reconstruction.

5.6. Detector Simulation Validation with Cosmic Ray Tracks

Finally, selected samples of cosmic ray tracks are compared in detail to a cosmic ray simulation based on the CORSIKA event generator and the detailed microphysical detector simulation introduced in Section 5. Starting from the cosmic ray track reconstruction described there, the track's start and end points are found by projecting the 3D points onto the cluster's principal components. The DBSCAN+RANSAC fit is applied on outlying hits until all are placed within a cluster or no hits remain. This is sufficient for studies of low-level detector response, as it provides a local approximation of the track trajectory with minimal impact from δ rays and hard scatters. Reconstructed tracks may show artificial gaps due to the presence of disabled channels. Also, cathode-piercing tracks will usually be reconstructed as separated tracks due to the non-zero cathode thickness. Thus, tracks with an angle smaller than 20° and closer than 10 cm are stitched together for the following analyses. A comparison between the spatial coordinates of the stitched tracks in data and simulation is shown in Figure 39.

Figure 40 shows a comparison of the dQ/dx for low-threshold and high-threshold runs with a sample of simulated cosmic rays. The dQ/dx has been measured for segments of different lengths following the procedure described in Section 5.6. The simulation assumes the Birks model for electron recombination and a gain of $4\,\mathrm{mV}/10^3\,\mathrm{e}^-$ [37]. In the data, the amount of charge that reaches the anode is corrected by the electron lifetime factor calculated in Section 5.1.

Next, the dQ/dx as a function of the reconstructed track residual range is considered. As noted in Section 5.5, for a muon that stops in the detector, the amount of deposited charge per unit length will increase as it approaches the end point, forming a Bragg peak. Figure 41 shows an example of a stopping muon and the subsequent Michel electron. The dQ/dx has been measured by subdividing the reconstructed track into 10 mm segments (our dx) and summing the charge contained in each segment (the dQ). The data show a Bragg peak near the end of the reconstructed track where the residual range is close to zero. The theoretical prediction is obtained by taking the $\langle \frac{dE}{dx} \rangle$ values tabulated in Ref. [44] for muons in LAr, divided by the argon ionization energy (23.6 eV), and multiplied by the recombination factor $R_{\mathrm{Birks}}^{\mathrm{ICARUS}}$, calculated in Ref. [38].

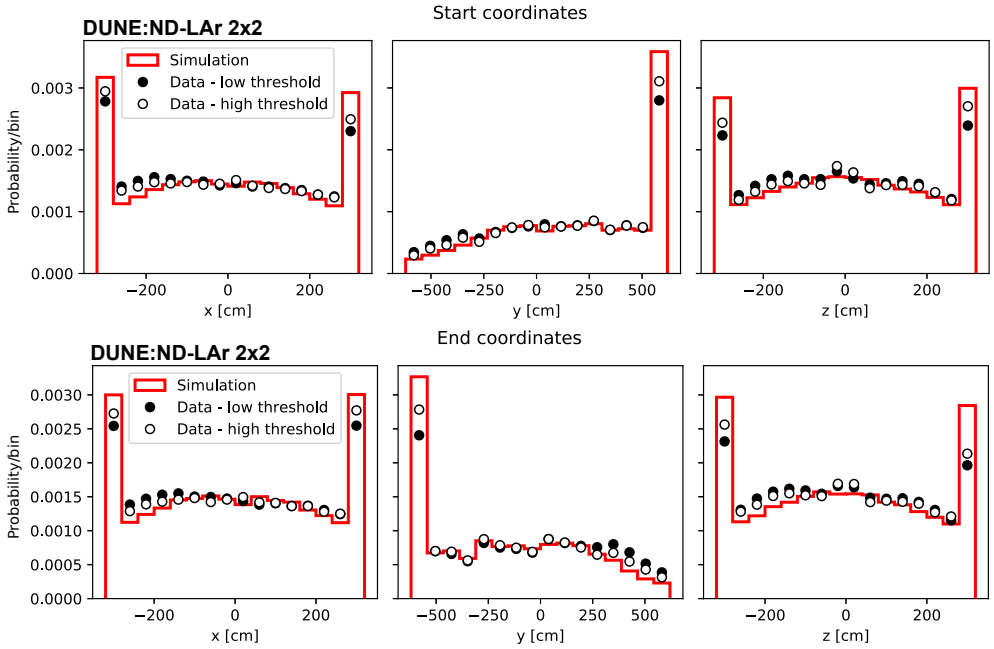

Figure 39. Start and end coordinates of stitched tracks in data (high- and low-threshold runs) and simulation.

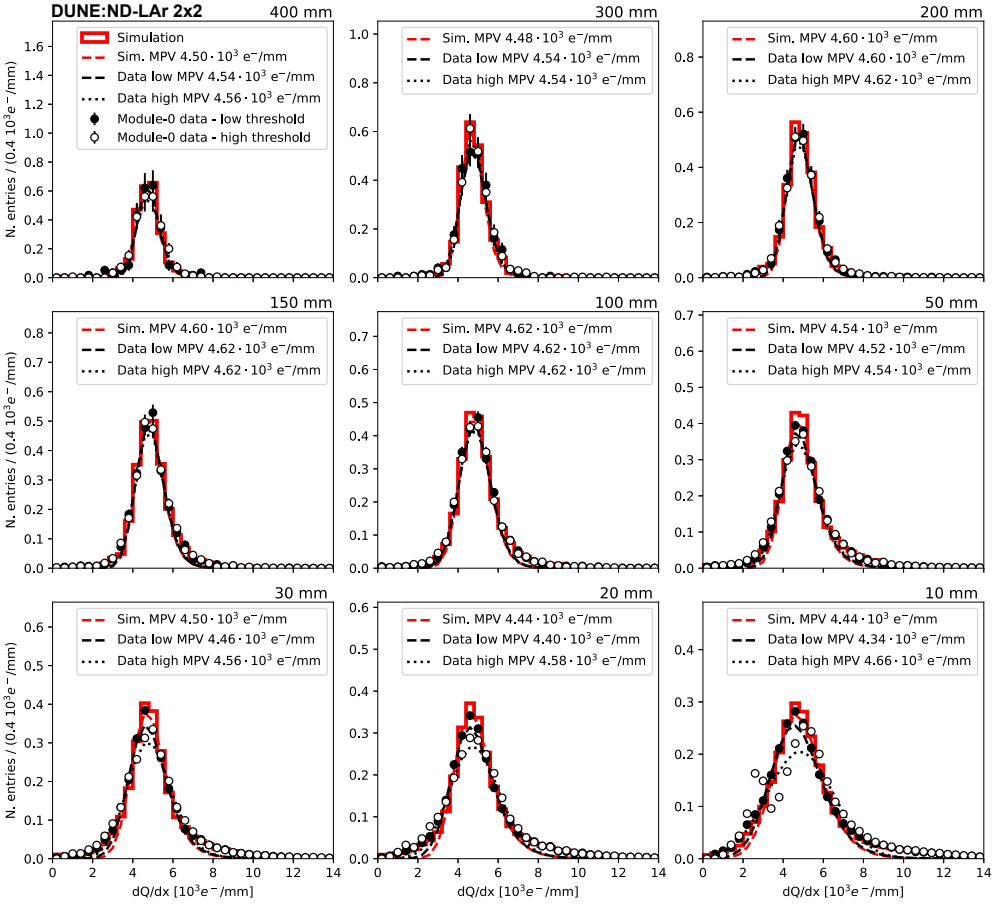

Figure 40. dQ/dx measured for segments of different lengths in low-threshold runs (black dots), high-threshold runs (white dots), and a sample of simulated cosmic rays (red line). The distributions have been fitted with a Gaussian-convolved Moyal function (dashed lines).

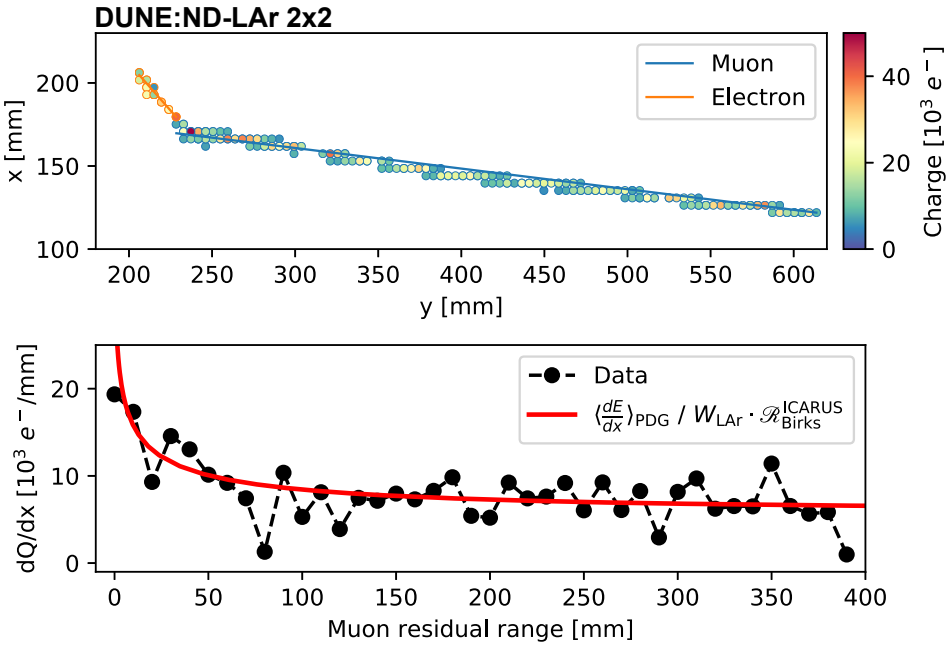

Figure 41. Top: Event display of the anode plane for a selected stopping muon (blue) and subsequent Michel electron (orange). **Bottom**: dQ/dx for the reconstructed muon track as a function of the residual range dQ/dx and the theoretical curve for muons stopping in liquid argon (red line).

The observed distributions indicate good overall agreement between data and simulations, in particular with the ability to correctly reproduce the position of the dQ/dx peak. Module-0 data provide input that can be used to further tune the detector simulation, including modeling of additional noise sources and details of the anode response. Meanwhile, the strong overall agreement in terms of vertex positioning and calorimetry indicates that the initial detector response model is able to capture the main features of the cosmic ray track samples.

6. Conclusions

We have reported here the experimental results of exposing the Module-0 demonstrator, a ton-scale LArTPC with pixel-based charge readout, to cosmic rays. This new type of neutrino detector is designed to meet the challenges of the near detector complex of the forthcoming DUNE experiment, which will be exposed to a very intense beam-related flux of particles. These challenges are expected to severely hamper the performance of a conventional, wire-readout, monolithic LArTPC, where reconstruction of complex 3D event topologies using a small number of 2D projections can lead to unsolvable ambiguities, particularly when multiple events overlap in the drift direction. The novel Module-0 design features a combination of new technological solutions: a pixelated anode to read out the ionization electron signal that provides native three-dimensional charge imaging, a modular structure with relatively short drift length, high-performance scintillation light detection systems, and an innovative approach to field shaping using a low-profile resistive shell. Module-0 is one of four units that will comprise the 2×2 demonstrator (ProtoDUNE-ND) being installed at Fermilab to be exposed to the NuMI neutrino beam.

A detailed assessment of this technology has been performed by operating Module-0, as well as the associated cryogenics, data acquisition, trigger, and timing infrastructure, at the University of Bern. A large sample of 25 million self-triggered cosmic ray-induced events was collected and analyzed along with an array of dedicated diagnostic data runs. The response of the 78,400-pixel readout system was studied as well as the performance of the two independent and complementary light detection systems. The data analysis demonstrated key physics requirements of this technology, such as the electron lifetime,

the uniformity of the electric field, and the matching/correlation between the charge and light signals. The reconstruction of particle tracks and Michel electrons illustrates the physics capabilities, and the comparison with detailed, microphysical simulations has demonstrated a robust understanding of the workings of this new type of LArTPC detector. Overall, these results demonstrate the key design features of the technique and provide a confirmation of the outstanding imaging capabilities of this next-generation LArTPC design.

Funding: This document was prepared by the DUNE collaboration using the resources of the Fermi National Accelerator Laboratory (Fermilab), a U.S. Department of Energy, Office of Science, HEP User Facility. Fermilab is managed by Fermi Research Alliance, LLC (FRA), acting under Contract No. DE-AC02-07CH11359. This work was supported by CNPq, FAPERJ, FAPEG, and FAPESP, Brazil; CFI, IPP, and NSERC, Canada; CERN; MŠMT, Czech Republic; ERDF, H2020-EU, and MSCA, European Union; CNRS/IN2P3 and CEA, France; INFN, Italy; FCT, Portugal; NRF, Republic of Korea; CAM, Fundación "La Caixa", Junta de Andalucía-FEDER, MICINN, and Xunta de Galicia, Spain; SERI and SNSF, Switzerland; TÜBİTAK, Turkey; The Royal Society and UKRI/STFC, UK; DOE and NSF, United States of America. This research used resources of the National Energy Research Scientific Computing Center (NERSC), a U.S. Department of Energy Office of Science User Facility operated under Contract No. DE-AC02-05CH11231.

Data Availability Statement: The datasets presented in this article are not readily available because the data are subject to restrictions per the DUNE collaboration policies and Data Management Plan. Inquiries regarding the data may be directed to the corresponding author.

Conflicts of Interest: The authors declare no conflict of interest.

References

1. Amerio, S.; Amoruso, S.; Antonello, M.; Aprili, P.; Armenante, M.; Arneodo, F.; Badertscher, A.; Baiboussinov, B.; Ceolin, M.B.; Battistoni, G.; et al. Design, construction and tests of the ICARUS T600 detector. *Nucl. Instrum. Meth. A* **2004**, *527*, 329–410. [CrossRef]
2. Anderson, C.; Antonello, M.; Baller, B.; Bolton, T.; Bromberg, C.; Cavanna, F.; Church, E.; Edmunds, D.; Ereditato, A.; Farooq, S.; et al. The ArgoNeuT Detector in the NuMI Low-Energy beam line at Fermilab. *J. Instrum.* **2012**, *7*, P10019. [CrossRef]
3. Acciarri, R.; Adams, C.; An, R.; Aparicio, A.; Aponte, S.; Asaadi, J.; Auger, M.; Ayoub, N.; Bagby, L.; Baller, B.; et al. Design and Construction of the MicroBooNE Detector. *J. Instrum.* **2017**, *12*, P02017. [CrossRef]
4. Abi, B.; Abud, A.A.; Acciarri, R.; Adamov, G.; Adamowski, M.; Adams, D.; Adrien, P.; Adinolfi, M.; Ahmad, Z.; Ahmed, J.; et al. First results on ProtoDUNE-SP liquid argon time projection chamber performance from a beam test at the CERN Neutrino Platform. *J. Instrum.* **2020**, *15*, P12004. [CrossRef]
5. Abud, A.A.; Abi, B.; Acciarri, R.; Adames, M.; Adamov, G.; Adams, D.; Adinolfi, M.; Aduszkiewicz, A.; Aguilar, J.; Ahmad, Z.; et al. Design, construction and operation of the ProtoDUNE-SP Liquid Argon TPC. *J. Instrum.* **2022**, *17*, P01005. [CrossRef]
6. Abi, B.; Acciarri, R.; Adamov, G.; Adams, D.; Adinolfi, M.; Ahmad, Z.; Ahmed, J.; Alion, T.; Monsalve, S.A.; Alt, C.; et al. Deep Underground Neutrino Experiment (DUNE), Far Detector Technical Design Report, Volume I Introduction to DUNE. *J. Instrum.* **2020**, *15*, T08008. [CrossRef]
7. DUNE Collaboration. Deep Underground Neutrino Experiment (DUNE) Near Detector Conceptual Design Report. *Instruments* **2021**, *5*, 31. [CrossRef]
8. Asaadi, J.; Auger, M.; Berner, R.; Bross, A.; Chen, Y.; Convery, M.; Domine, L.; Drielsma, F.; Dwyer, D.; Ereditato, A.; et al. A New Concept for Kilotonne Scale Liquid Argon Time Projection Chambers. *Instruments* **2020**, *4*, 6. [CrossRef]
9. Dwyer, D.; Garcia-Sciveres, M.; Gnani, D.; Grace, C.; Kohn, S.; Kramer, M.; Krieger, A.; Lin, C.; Luk, K.; Madigan, P.; et al. LArPix: Demonstration of low-power 3D pixelated charge readout for liquid argon time projection chambers. *J. Instrum.* **2018**, *13*, P10007. [CrossRef]
10. Russell, B.; et al. The 2 × 2 Demonstrator—A demonstrator for the DUNE ND-LAr Near Detector based on the ArgonCube Design. *Proc. Sci.* **2024**, *TAUP2023*, 221. [CrossRef]
11. Auger, M.; Chen, Y.; Ereditato, A.; Goeldi, D.; Kreslo, I.; Lorca, D.; Luethi, M.; Mettler, T.; Sinclair, J.; Weber, M. ArCLight—A Compact Dielectric Large-Area Photon Detector. *Instruments* **2018**, *2*, 3. [CrossRef]
12. Anfimov, N.; Berner, R.; Butorov, I.; Chetverikov, A.; Fedoseev, D.; Gromov, B.; Korablev, D.; Kreslo, I.; Kuznetsova, K.; Olshevskiy, A.; et al. Development of the Light Collection Module for the Liquid Argon Time Projection Chamber (LArTPC). *J. Instrum.* **2020**, *15*, C07022. [CrossRef]
13. Berner, R.; Chen, Y.; Ereditato, A.; Koller, P.P.; Kreslo, I.; Lorca, D.; Mettler, T.; Miao, T.; Piastra, F.; Sinclair, J.R.; et al. First Operation of a Resistive Shell Liquid Argon Time Projection Chamber: A New Approach to Electric-Field Shaping. *Instruments* **2019**, *3*, 28. [CrossRef]

14. Adamson, P.; Anderson, K.; Andrews, M.; Andrews, R.; Anghel, I.; Augustine, D.; Aurisano, A.; Avvakumov, S.; Ayres, D.; Baller, B.; et al. The NuMI Neutrino Beam. *Nucl. Instrum. Meth. A* **2016**, *806*, 279–306. [CrossRef]
15. Asaadi, J.; Auger, M.; Ereditato, A.; Goeldi, D.; Kose, U.; Kreslo, I.; Lorca, D.; Luethi, M.; Von Rohr, C.B.U.R.; Sinclair, J.; et al. First Demonstration of a Pixelated Charge Readout for Single-Phase Liquid Argon Time Projection Chambers. *Instruments* **2020**, *4*, 9. [CrossRef]
16. Asaadi, J.; Auger, M.; Ereditato, A.; Goeldi, D.; Hänni, R.; Kose, U.; Kreslo, I.; Lorca, D.; Luethi, M.; von Rohr, C.R.; et al. A pixelated charge readout for Liquid Argon Time Projection Chambers. *J. Instrum.* **2018**, *13*, C02008. [CrossRef]
17. Machado, A.; Segreto, E. ARAPUCA a new device for liquid argon scintillation light detection. *J. Instrum.* **2016**, *11*, C02004. [CrossRef]
18. Serrano, J.; Gaderer, G.; Loschmidt, P.; Cota, E.G.; Lewis, J.H.; Cattin, M.; Alvarez, P.; Oliveira Fernandes Moreira, P.M.; Wlostowski, T.; Dedic, J.; et al. The White Rabbit Project. In Proceedings of the Proc. 12th Int. Conf. on Accelerator and Large Experimental Physics Control Systems (ICALEPCS'09), Kobe, Japan, 12–16 October 2009; JACoW Publishing: Geneva, Switzerland , 2009; pp. 93–95.
19. Ester, M.; Kriegel, H.P.; Sander, J.; Xu, X. *A Density-Based Algorithm for Discovering Clusters in Large Spatial Databases with Noise*; KDD'96; AAAI Press: Washington, DC, USA, 1996.
20. Moyal, J. XXX. Theory of ionization fluctuations. *Lond. Edinb. Dublin Philos. Mag. J. Sci.* **1955**, *46*, 263–280. [CrossRef]
21. Baller, B. Liquid Argon Properties (Tables and Calculators) Version 4. Available online: https://lar.bnl.gov/properties/ (accessed on 1 July 2021).
22. Hamamatsu. MPPC S13360 Series Datasheet. Available online: https://www.hamamatsu.com/resources/pdf/ssd/s13360_series_kapd1052e.pdf (accessed on 1 July 2021).
23. Heck, D.; Knapp, J.; Capdevielle, J.N.; Schatz, G.; Thouw, T. *CORSIKA: A Monte Carlo Code to Simulate Extensive Air Showers*; Forschungszentrum Karlsruhe Report FZKA 6019 (1998); Forschungszentrum Karlsruhe GmbH: Karlsruhe, Germany, 1998.
24. Agostinelli, S.; Allison, J.; Amako, K.; Apostolakis, J.; Araujo, H.; Arce, P.; Asai, M.; Axen, D.; Banerjee, S.; Barrand, G.; et al. Geant4—A simulation toolkit. *Nucl. Instrum. Methods Phys. Res. Sect. Accel. Spectrometers Detect. Assoc. Equip.* **2003**, *506*, 250–303. [CrossRef]
25. Soleti, S.R.; Dwyer, D.; Vallari, Z. DUNE/larnd-sim. Available online: https://zenodo.org/records/4582721 (accessed on 25 August 2022).
26. Abud, A.A.; Abi, B.; Acciarri, R.; Acero, M.; Adames, M.; Adamov, G.; Adamowski, M.; Adams, D.; Adinolfi, M.; Adriano, C.; et al. Highly-parallelized simulation of a pixelated LArTPC on a GPU. *J. Instrum.* **2023**, *18*, P04034. [CrossRef]
27. Fischler, M.A.; Bolles, R.C. Random Sample Consensus: A Paradigm for Model Fitting with Applications to Image Analysis and Automated Cartography. *Commun. ACM* **1981**, *24*, 381–395. [CrossRef]
28. Adams, C.; Alrashed, M.; An, R.; Anthony, J.; Asaadi, J.; Ashkenazi, A.; Balasubramanian, S.; Baller, B.; Barnes, C.; Barr, G.; et al. Calibration of the charge and energy loss per unit length of the MicroBooNE liquid argon time projection chamber using muons and protons. *J. Instrum.* **2020**, *15*, P03022. [CrossRef]
29. Bettini, A.; Braggiotti, A.; Casagrande, F.; Casoli, P.; Cennini, P.; Centro, S.; Cheng, M.; Ciocio, A.; Cittolin, S.; Cline, D.; et al. A study of the factors affecting the electron lifetime in ultra-pure liquid argon. *Nucl. Instrum. Methods Phys. Res. Sect. Accel. Spectrometers Detect. Assoc. Equip.* **1991**, *305*, 177–186. [CrossRef]
30. Abi, B.; Acciarri, R.; Adamov, G.; Adams, D.; Adinolfi, M.; Ahmad, Z.; Ahmed, J.; Alion, T.; Monsalve, S.A.; Alt, C.; et al. Deep Underground Neutrino Experiment (DUNE), Far Detector Technical Design Report, Volume IV: Far Detector Single-phase Technology. *J. Instrum.* **2020**, *15*, T08010. [CrossRef]
31. Abratenko, P.; Alrashed, M.; An, R.; Anthony, J.; Asaadi, J.; Ashkenazi, A.; Balasubramanian, S.; Baller, B.; Barnes, C.; Barr, G.; et al. Measurement of space charge effects in the MicroBooNE LArTPC using cosmic muons. *J. Instrum.* **2020**, *15*, P12037. [CrossRef]
32. Skwarnicki, T. A study of the Radiative CASCADE Transitions between the Upsilon-Prime and Upsilon Resonances. F31-86-02. Ph.D. Thesis, DESY, Hamburg, Germany, 1986.
33. Oreglia, M.J. A Study of the Reactions $\psi' \to \gamma\gamma\psi$. SLAC-R-236. Ph.D. Thesis, Stanford Linear Accelerator Center, Stanford, CA, USA, 1980.
34. Gaiser, J.E. Charmonium Spectroscopy from Radiative Decays of the J/ψ and ψ'^*. SLAC-R-255. Ph.D. Thesis, Stanford Linear Accelerator Center, Stanford, CA, USA, 1982.
35. Shibamura, E.; Hitachi, A.; Doke, T.; Takahashi, T.; Kubota, S.; Miyajima, M. Drift velocities of electrons, saturation characteristics of ionization and W-values for conversion electrons in liquid argon, liquid argon-gas mixtures and liquid xenon. *Nucl. Instrum. Meth.* **1975**, *131*, 249–258. [CrossRef]
36. Thomas, J.; Imel, D.A. Recombination of electron-ion pairs in liquid argon and liquid xenon. *Phys. Rev. A* **1987**, *36*, 614–616. [CrossRef] [PubMed]
37. Birks, J.B. Scintillations from Organic Crystals: Specific Fluorescence and Relative Response to Different Radiations. *Proc. Phys. Soc. A* **1951**, *64*, 874–877. [CrossRef]
38. Amoruso, S.; Antonello, M.; Aprili, P.; Arneodo, F.; Badertscher, A.; Baiboussinov, B.; Ceolin, M.B.; Battistoni, G.; Bekman, B.; Benetti, P.; et al. Study of electron recombination in liquid argon with the ICARUS TPC. *Nucl. Instrum. Meth. A* **2004**, *523*, 275–286. [CrossRef]

39. Acciarri, R.; Adams, C.; Asaadi, J.; Baller, B.; Bolton, T.; Bromberg, C.; Cavanna, F.; Church, E.; Edmunds, D.; Ereditato, A.; et al. A study of electron recombination using highly ionizing particles in the ArgoNeuT Liquid Argon TPC. *J. Instrum.* **2013**, *8*, P08005. [CrossRef]
40. Doke, T.; Hitachi, A.; Kikuchi, J.; Masuda, K.; Okada, H.; Shibamura, E. Absolute Scintillation Yields in Liquid Argon and Xenon for Various Particles. *Jpn. J. Appl. Phys.* **2002**, *41*, 1538. [CrossRef]
41. Abud, A.A.; Abi, B.; Acciarri, R.; Acero, M.A.; Adames, M.R.; Adamov, G.; Adamowski, M.; Adams, D.; Adinolfi, M.; Adriano, C.; et al. Identification and reconstruction of low-energy electrons in the ProtoDUNE-SP detector. *Phys. Rev. D* **2023**, *107*, 092012. [CrossRef]
42. Foreman, W.; Acciarri, R.; Asaadi, J.A.; Badgett, W.; Blaszczyk, F.D.M.; Bouabid, R.; Bromberg, C.; Carey, R.; Cavanna, F.; Aleman, J.I.C.; et al. Calorimetry for low-energy electrons using charge and light in liquid argon. *Phys. Rev. D* **2020**, *101*, 012010. [CrossRef]
43. Acciarri, R.; Adams, C.; An, R.; Anthony, J.; Asaadi, J.; Auger, M.; Bagby, L.; Balasubramanian, S.; Baller, B.; Barnes, C.; et al. Michel Electron Reconstruction Using Cosmic-Ray Data from the MicroBooNE LArTPC. *J. Instrum.* **2017**, *12*, P09014. [CrossRef]
44. Groom, D.E.; Mokhov, N.V.; Striganov, S.I. Muon stopping power and range tables 10-MeV to 100-TeV. *Atom. Data Nucl. Data Tabl.* **2001**, *78*, 183–356. [CrossRef]